Optimization of High Efficiency Thermoelectrics based on Tl_5Te_3

Optimierung von Hochleistungs-Thermoelektrika auf Tl_5Te_3-Basis

Diplomarbeit

Jens Thilo Teubner
Höll 13, 88069 Tettnang
jens.teubner@uni-konstanz.de

März 2001

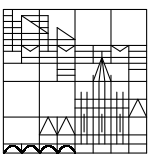

Universität Konstanz
Fachbereich Physik

Lucent Technologies
Bell Labs Innovations

Abstract

The Tl_5Te_3 related compounds have recently been discovered as very efficient materials for thermoelectric applications [Wolfing00]. In this work, techniques have been investigated to further optimize materials in this group. The compound Tl_9SbTe_6 was characterized and found to exhibit very good thermoelectric performance, although it stays behind Tl_9BiTe_6, which still has to be considered as the best ternary compound in the Tl_5Te_3 group.

Investigations on the Tl_9SbTe_6–Tl_9BiTe_6 alloy system have been carried out in order to optimize the electronic properties and lower the lattice thermal conductivity. Measurements and theoretical estimations show that an optimized material must be at or close to the Tl_9BiTe_6 end of the system. The expected improvement due to a reduction of the thermal conductivity by alloy scattering, however, was not observed.

A study on the effect of doping in Tl_9BiTe_6 was carried out. By doping with bismuth *n*-type Tl_9BiTe_6 could be prepared, which would be necessary for a thermoelectric device that is solely based on Tl_9BiTe_6. Unfortunately, *n*-type Tl_9BiTe_6 was found to have much weaker thermoelectric performance than its *p*-type counterpart.

Doping experiments with HgTe showed that *p*-type doping can improve the performance of Tl_9BiTe_6. However, a significant embrittlement has been observed on this material, that limits its use in actual devices. Further optimization of the doping technique and/or the dopant itself are expected to solve these problems and enhance the performance of Tl_9BiTe_6.

In additional investigations YNiSb- and $Zr_3Ni_3Sb_4$-related compounds have been screened for their thermoelectric properties. The members of both groups exhibit high thermopowers and have low thermal conductivities. The high electrical resistivity, however, limits the thermoelectric performance. Nevertheless, further research in related systems seems promising.

Zusammenfassung

Einige Materialien der Tl_5Te_3-Gruppe wurden vor kurzem als hocheffizient für thermoelektrische Anwendungen identifiziert [Wolfing00]. In dieser Arbeit wurden Techniken untersucht, um die Materialien aus dieser Gruppe weiter zu optimieren. Die Verbindung Tl_9SbTe_6 wurde charakterisiert und als Material mit sehr guten thermoelektrischen Eigenschaften identifiziert. Es bleibt jedoch hinter Tl_9BiTe_6 zurück, der besten ternären Verbindung in der Tl_5Te_3-Gruppe.

Untersuchungen an dem Legierungs-System Tl_9SbTe_6–Tl_9BiTe_6 wurden unternommen, um die elektronischen Eigenschaften zu optimieren und die Wärmeleitfähigkeit zu reduzieren. Messungen und theoretische Abschätzungen zeigen, daß ein optimiertes Material in der Nähe der Verbindung Tl_9BiTe_6 zu suchen ist. Die erhoffte Verbesserung durch eine Reduktion der Wärmeleitfähigkeit aufgrund von Legierungseffekten wurde jedoch nicht beobachtet.

Der Einfluß verschiedener Dotierungen auf die thermoelektrischen Eigenschaften von Tl_9BiTe_6 wurde untersucht. Durch Dotierung mit Bismut konnte n-typ Tl_9BiTe_6 hergestellt werden, das für die Herstellung eines reinen Tl_9BiTe_6-Bauelements notwendig wäre. Es stellt sich jedoch heraus, daß n-typ Tl_9BiTe_6 deutlich schlechtere thermoelektrische Eigenschaften zeigt als sein p-typ Gegenstück.

Durch Dotierversuche mit HgTe wurde nachgewiesen, daß eine p-Dotierung den Wirkungsgrad von Tl_9BiTe_6 verbessern kann. Allerdings zeigten sich Probleme mit der mechanischen Stabilität, die das Material nur begrenzt in der Praxis einsetzbar machen. Es scheint wahrscheinlich, daß diese Probleme durch eine weitere Optimierung der Dotiertechnik und/oder des Dotanden gelöst werden können und die Leistungsfähigkeit von Tl_9BiTe_6 weiter verbessert werden kann.

In einer weiteren Studie wurden YNiSb- und $Zr_3Ni_3Sb_4$-verwandte Verbindungen auf ihre thermoelektrischen Eigenschaften untersucht. In beiden Gruppen wurden hohe Seebeckkoeffizienten und niedrige Wärmeleitfähigkeiten beobachtet, der Wirkungsgrad ist jedoch aufgrund der zu hohen elektrischen Widerstände zu gering. Die Gruppen an sich bleiben jedoch weiterhin vielversprechend und es scheint durchaus lohnenswert, in Zukunft weitere Materialien dieser Gruppen zu untersuchen.

Contents

1 Introduction

We've all become used to it, to this quietly humming sound that emerges from our kitchen at night, when everything else is quiet. It is the compressor in our refrigerator, working hard to keep the ice cream frozen and the milk cold. Heat is scooped out of the inside and dumped to the outside by constantly evaporating and condensing a fluid — often a chlorofuorocarbon, known for its ozon-destructing effect in the atmosphere. Imagine this is all replaced by a technique that is absolutely silent, lightweight and extremely reliable...

In principle, this is possible since over 150 years, when Thomas Seebeck and Jean-Charles-Athanase Peltier discovered the first *thermoelectric effects* (1821 and 1834, resp.). With this effect electrical energy can be directly converted to a heat separation, or — vice versa — a temperature difference is converted into electrical energy.

Heinrich Lenz already proved this possibility in 1838, when he froze a drop of water on a junction of bismuth and antimony wires. But thermoelectricity remained little more than a curiosity until the 1950s, when Abraham Ioffe found that doped semiconductors had a much larger thermoelectric effect than did other materials.

His discovery started a frenzy of research activities. Very early remarkable performances were achieved, and scientists were spured by the success of Bi_2Te_3, which was found as an efficient material. Military interests further drove the research efforts.

Thermoelectricity promised some revolutionizing features, compared to conventional compressor techniques:

- Thermoelectric coolers/generators don't need any moving parts. This makes them absolutely *silent* and extremely *reliable*.
- Thermoelectric devices are *small* and *lightweight*. This makes them interesting for applications like portable camping coolers and for portable electronics, i. e. laptops, etc.
- The *scalability* of the devices is the key feature in the microelectronics and communications area. Thermoelectrics are used to cool microprocessors or stabilize

the temperature in optical systems to increase bandwidth.

As the real breakthrough stayed away and no better materials than Bi_2Te_3 were found, research activities calmed down. It seemed that virtually every known semiconductor was evaluated and Bi_2Te_3 was the best material. As compressor based units are still three times more efficient, thermoelectric devices are still a niche market. The market for thermoelectric devices today is about $120 million a year, mainly spent for cooling laser diodes and picnic baskets. Other usages are the energy supply of some deep space satellites (because of the high reliability) and the recent presentation of a wrist watch, powered by the heat of the human body.

Seiko's "Thermic", the first wristwatch powered by the thermoelectric effect.

In the recent years, however, the field experienced a rebirth. New compounds were synthesized with large and complex unit cells that promise interesting thermoelectric performance. At the same time, new demands for solid-state cooling emerged. For the upcoming microelectronic and communication technology, thermoelectric cooling is the ideal choice. Faster microprocessors need to be cooled and the high bandwidth in optical communication systems can only be achieved with temperature stabilized lasers. For this increasing demand, new thermoelectric materials with higher efficiency are strongly needed.

Recently, the Tl_5Te_3 group has been discovered as a group of highly efficient thermoelectric materials [Wolfing00]. One of the compounds of this group outperforms all known *p*-type compounds in the temperature range from 400 to 450 Kelvin. So far only little optimization has been carried out, and further investigation of these compounds may lead to higher efficiencies and/or lower operating temperatures, which would be important for cooling applications.

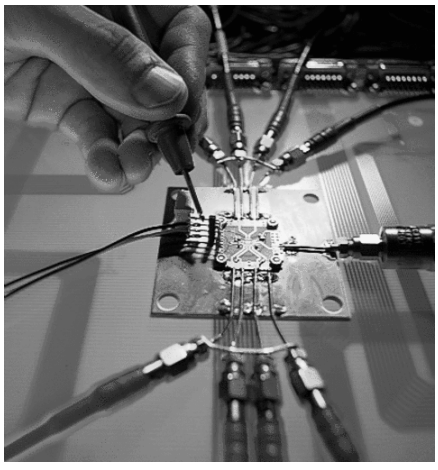

Thermoelectric cooling could enhance the performance of modern high-speed electronics.

The goal of this work is to investigate different approaches to further optimize the Tl_5Te_3 group. After a theoretical introduction in the next chapter a short overview is presented of the techniques used in this work to measure the thermoelectric properties.

As a basis for further optimizations, an overview of the Tl_5Te_3 group is given in chapter 4. Known properties and recent results in the literature are summarized in this chapter. This leads to two main techniques to optimize the materials. The effect of forming solid solutions in the group is discussed after the characterization of Tl_9SbTe_6, a representative of the group.

Subsequently, doping experiments are carried out on the most successful compound in the group, Tl_9BiTe_6. By doping the charge carrier density can be fine-tuned to optimize the thermoelectric figure

of merit, $ZT = S^2\sigma T/\kappa$.

Additionally, another two classes of materials have been investigated. Some materials with the Half-Heusler structure have already shown interesting thermoelectric performance recently [Hohl97]. The YNiSb and $Zr_3Ni_3Sb_4$ related compounds, however, had not been investigated so far. In chapters 8 and 9 compounds of these groups have been synthesized and evaluated. Another aspect of the two chapters are the effects of doping and alloying in these groups.

To close the work, the results are summarized and evaluated. An outlook gives prospects for future research on related materials.

2 Theory of Thermoelectric Effects

2.1 Introduction and Definitions

In 1821 Thomas Seebeck discovered the first thermoelectric effect, the *Seebeck effect* [Seebeck22]. A couple of years later two more effects were discoverd: the *Peltier effect* and the *Thomson effect* [Peltier34, Thomson51]. All three effects are related to each other by the *Kelvin relations*.

2.1.1 The Seebeck Effect

The Seebeck effect is defined by a circuit as shown in figure 2.1, which shows two conductors a and b with junctions at A and B. A temperature difference ΔT is established between these two junctions.

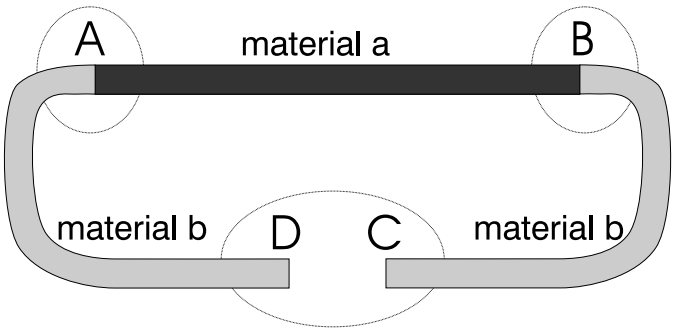

Figure 2.1: Circuit used in defining the thermoelectric coefficients. The circles symbolize regions of same temperature. If a temperature difference is applied between A and B, a Seebeck voltage can be measured between the points C and D.

Under these conditions, an open-circuit voltage V between C and D can be measured that follows the equation

$$S_{ab} = \frac{V}{\Delta T} \tag{2.1}$$

which defines the Seebeck coefficient S_{ab} for a junction of the materials a and b.

With this approach only a differential Seebeck coefficient for a pair of materials can be defined. It would clearly be more convenient to have an absolute Seebeck coefficient that can be assigned to only one material. The differential Seebeck coefficient S_{ab} would then be $S_{ab} = S_a - S_b$ where S_a and S_b are the absolute coefficient of material a and b, respectively.

This is in fact possible with the use of superconductors as a reference material. All superconductors exhibit a Seebeck coefficient of zero below their critical temperature.

2.1.2 The Peltier Effect

To define the Peltier effect, the same circuit in figure 2.1 is used. Both points A and B are at the same temperature. If now a current (current density $\mathbf{j}$) is made to flow through the circuit, heat will be transported from one end of the sample to the other. The proportional constant Π_{ab} in

$$\mathbf{w} = \Pi_{ab}\mathbf{j} \tag{2.2}$$

is defined as the Peltier coefficient ($\mathbf{w}$ is the heat flow). Again an absolute Peltier coefficient can be defined with the use of superconductors.

2.1.3 The Thomson Effect

To observe the Thomson effect, one material is sufficient. If an electrical current flows through a material that has a temperature gradient, heat is transported. The Tomson coefficient τ is defined by the equation

$$\mathbf{w} = \tau\,\mathbf{j}\,\nabla T\,. \tag{2.3}$$

2.1.4 The Kelvin Relations

The three transport parameters introduced above are not independent. The theory of irreversible thermodynamics proves the validity of the *Kelvin relations*

$$\Pi_{ab} = S_{ab}T \tag{2.4}$$

$$\tau_a - \tau_b = T\frac{dS_{ab}}{dT}\,. \tag{2.5}$$

2.2 Efficiency

The maximum efficiency of a thermoelectric power generation device was calculated by Ioffe in 1957 [Ioffe57]:

$$\eta_{\max} = \underbrace{\frac{T_\mathrm{H} - T_\mathrm{C}}{T_\mathrm{H}}}_{\eta_\mathrm{Carnot}} \frac{\sqrt{1+ZT}-1}{\sqrt{1+ZT}+\frac{T_\mathrm{C}}{T_\mathrm{H}}}\,. \tag{2.6}$$

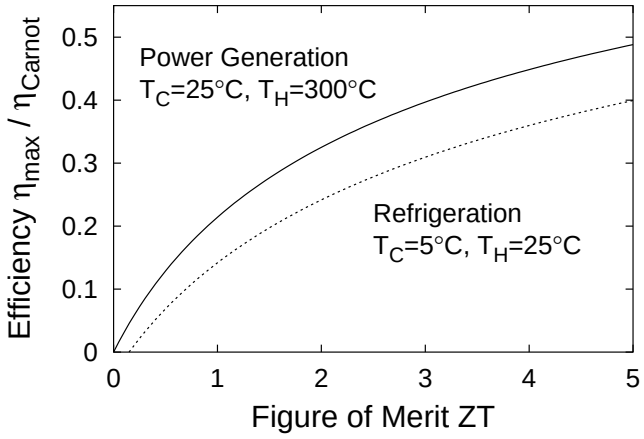

Figure 2.2: Correlation between the efficiency of a thermoelectric device and the Carnot efficiency for two typical examples.

T_C and T_H denote the absolute temperature at the cold and on the hot end, respectively, T is the mean temperature. Z is the *thermoelectric figure of merit*

$$Z = \frac{S^2\sigma}{\kappa} \tag{2.7}$$

with the Seebeck coefficient S, the electrical conductivity σ and the thermal conductivity κ.

If the thermoelectric device is used for refrigeration a similar expression is obtained:

$$\eta_\mathrm{max} = \underbrace{\frac{T_\mathrm{H}}{T_\mathrm{H} - T_\mathrm{C}}}_{\eta_\mathrm{Carnot}} \frac{\sqrt{1+ZT} - \frac{T_\mathrm{H}}{T_\mathrm{C}}}{\sqrt{1+ZT}+1} \,. \tag{2.8}$$

As seen in this equations, the efficiency only depends on the dimensionless figure of merit ZT, where a higher ZT results in a higher efficiency. The maximum obtainable efficiency is the Carnot efficiency η_Carnot which is obtained for $ZT \to \infty$.

The correlation between the dimesionless figure of merit and the Carnot efficiency is given in figure 2.2 for two typical applications. For refrigeration a household refrigerator is considered, whereas for power generation the application could be heat recovery from an engine in a car.

To allow a systematic search for good thermoelectric materials, the transport parameters S, σ and κ have to be expressed by more fundamental properties. In the following sections not only the dependence on parameters like energy gap or carrier concentration will be shown. Attempts are also made to relate these parameters to practically useful parameters like crystal structure or the constituing elements.

2.3 Transport Theory

2.3.1 The Boltzmann Equation

In the unperturbed equilibrium state with no electric field or temperature gradient the charge carrier distribution in a material is given by the *Fermi-Dirac distribution function*[1]:

$$f_0(E) = \frac{1}{\exp\left(\frac{E-E_\mathrm{F}}{k_\mathrm{B}T}\right)+1} \tag{2.9}$$

where E_F denotes the Fermi energy, k_B is Boltzmann's constant and T the absolute temperature. E is the energy of the charge carrier.

Under the presence of electrical fields or a temperature gradient this distribution is no longer valid. To explain electrical conduction or thermoelectric effects, we therefore have to calculate a perturbed distribution f, which we assume is not too far away from the unperturbed Fermi-Dirac distribution.

If the system is not in the equilibrium state, scattering of the electrons on lattice defects, phonons, etc. will force the distribution back to its equilibrium state. The rate of change of the distribution function will be proportional to its difference to the equilibrium distribution. The constant of proportionality is the *relaxation time* τ. The equation to describe this relaxation process is the *Boltzmann equation*:

$$\frac{df(E)}{dt} = \frac{f(E)-f_0(E)}{\tau(E)}\,. \tag{2.10}$$

In most cases, the energy dependence of τ can be expressed by a power law of the form

$$\tau(E) = \tau_0(T)E^r \tag{2.11}$$

where the exponent r depends on the scattering mechanism. Therefore r is called the *scattering parameter*. In most cases the exponent r is the important variable, rather than the factor τ_0.

If the electrical field and the temperature gradient lie along the x-axis, the left side of (2.10) reduces to

$$\frac{df}{dt} = \frac{\partial f}{\partial t} + \frac{\partial f}{\partial E}\frac{\partial E}{\partial t} + \frac{\partial f}{\partial x}v_x = -\frac{\partial f_0}{\partial E}v_x\left[\frac{\partial E_\mathrm{F}}{\partial x} + \frac{E-E_\mathrm{F}}{T}\frac{\partial T}{\partial x}\right]. \tag{2.12}$$

In the last step f was replaced with f_0 under the assumption that $f - f_0 \ll f_0$. $\frac{\partial x}{\partial t}$ denotes the carrier velocity and was written as v_x. The partial derivation of f with respect to time was neglected, because the system is assumed to be in a steady state. Because of $f = f(E - E_\mathrm{F})$, $\frac{\partial f}{\partial E_\mathrm{F}}$ equals $-\frac{\partial f}{\partial E}$.

Combining equations (2.10) and (2.12) we receive an expression for the distribution function f:

$$f = f_0 - \tau\frac{\partial f_0}{\partial E}v_x\left[\frac{\partial E_\mathrm{F}}{\partial x} + \frac{E-E_\mathrm{F}}{T}\frac{\partial T}{\partial x}\right]. \tag{2.13}$$

[1] see e. g. [Spears01, formula 1.14]

2.3.2 Electrical Conduction

The current density $\mathbf{j}$ in a material is equal to the velocity of the charge carriers times their charge summed over all the carriers:[2]

$$\mathbf{j} = \mp e \int \mathbf{v}(E) f(E) g(E)\, dE \tag{2.14}$$

where $g(E)\, dE$ is the number of allowed electronic states with energies between E and $E + dE$ (density of states). For free electrons, $g(E)$ is given by[3]

$$g(E) = \frac{4\pi (2m^*)^{3/2} E^{1/2}}{h^3}\,. \tag{2.15}$$

If again only the x direction is considered, (2.14) evaluates with (2.13) to

$$j_x = \pm e \int \tau \frac{\partial f_0}{\partial E} v_x^2 \left[\frac{\partial E_\mathrm{F}}{\partial x} + \frac{E - E_\mathrm{F}}{T} \frac{\partial T}{\partial x} \right] g(E)\, dE\,. \tag{2.16}$$

The f_0 term was neglected because it does not contribute to the net current.

For the calculation of the electrical conduction we are only interested in the first term in the brackets. There shall be no temperature gradient along the sample. In (2.16) the special form of τ from equation (2.11) is inserted. The energy of an electron with velocity $\mathbf{v}$ is $\frac{1}{2} m^* \mathbf{v}^2$. Since the thermal velocity greatly exceeds the drift velocity, it is uniform in all directions and we can replace

$$v_x^2 = \frac{2E}{3m^*}\,. \tag{2.17}$$

With partial integration of (2.16) we obtain

$$j_x = \pm \frac{8^{3/2} e \tau_0 \pi m^{*1/2}}{h^3} \frac{\partial E_\mathrm{F}}{\partial x} \left(r + \frac{3}{2} \right) \int E^{r+1/2} f_0(E)\, dE\,. \tag{2.18}$$

The form of the integral in equation (2.18) is similar to the *Fermi integral*

$$F_j(\varepsilon) = \int_0^\infty \frac{x^j}{\exp(x - \varepsilon) + 1}\, dx \tag{2.19}$$

which is a frequently used function in semiconductor physics. In some textbooks the Fermi integrals are normalized by a factor $\frac{1}{j!}$. In this thesis, the definition (2.19) will be used.

Another common abbreviation are the integrals

$$K_i = -\frac{8^{3/2}\pi}{3h^3 k_\mathrm{B} T} m^{*1/2} \tau_0 \left(i + \frac{3}{2} \right) \int E^{i+1/2} f_0(E)\, dE\,. \tag{2.20}$$

[2] The sign depends on the type of charge carriers (electrons/holes).

[3] For free electrons m^* is the free electron mass m_e. For parabolic bands, m_e has to be replaced by an effective mass m^*.

Rewriting (2.18) with Fermi integrals yields

$$j_x = \pm \frac{e\tau_0 8^{3/2}\pi m^{*1/2}}{h^3} (k_\mathrm{B}T)^{r+3/2} \left(r + \frac{3}{2}\right) F_{r+1/2}(\varepsilon_\mathrm{F}) \frac{\partial E_\mathrm{F}}{\partial x} . \tag{2.21}$$

The quantity ε_F denotes the reduced Fermi energy $\frac{E_\mathrm{F}}{k_\mathrm{B}T}$. The gradient of the Fermi energy, $\frac{\partial E_\mathrm{F}}{\partial x}$ corresponds to the electric field

$$\frac{\partial E_\mathrm{F}}{\partial x} = \pm e\mathsf{E}_x . \tag{2.22}$$

With the defining equation for the electrical conductivity

$$\mathbf{j} = \sigma\mathsf{E} \tag{2.23}$$

the conductivity can be evaluated to

$$\sigma = e^2 K_r \tag{2.24}$$

$$= \frac{e^2\tau_0 8^{3/2}\pi m^{*1/2}}{h^3} (k_\mathrm{B}T)^{r+3/2} \left(r + \frac{3}{2}\right) F_{r+1/2}(\varepsilon_\mathrm{F}) . \tag{2.25}$$

2.3.3 Charge Carrier Density and Mobility

The electrical conductivity obviously strongly depends on the number of free charge carriers n. The factor of proportionality between the two quantities is the *mobility* μ. It is defined by the equation

$$\sigma = e\mu n \tag{2.26}$$

with e denoting the elementary charge.

The charge carrier density can be calculated by multiplying the density of states $g(E)$ (see eq. 2.15) with the distribution function $f(E)$ and integrating over all energies. For parabolic bands this results in

$$n = 2 \left(\frac{m^* k_\mathrm{B}T}{2\pi\hbar^2}\right)^{3/2} F_{1/2}(\varepsilon_\mathrm{F}) . \tag{2.27}$$

The charge carrier mobility μ can be determined by dividing σ by μ.

2.3.4 Heat Conduction — Electronic Part

Thermal conduction is defined by the equation

$$\mathbf{w} = -\kappa\nabla T \tag{2.28}$$

where $\mathbf{w}$ is the *heat flow* through the material, the equivalent to the current density in the electrical case and κ is the *thermal conductivity*. It consists of two main parts: heat transported by electrons moving through the crystals (electrical contribution) and thermal excitation of lattice vibrations (lattice contribution). In this section the electronic contribution will be discussed.

On their way through the crystal, electrons not only transport charge. They also carry an amount of energy which is reflected as transport of heat. Therefore the heat flow $\mathbf{w}$ is described by

$$\begin{aligned}\mathbf{w} &= \int \mathbf{v}(E)(E - E_\mathrm{F}) f(E) g(E)\, dE \\ &= \pm \frac{E_\mathrm{F}}{e}\mathbf{j} + \int \tau \frac{\partial f_0}{\partial E}\mathbf{v}(E)E\left[\frac{\partial E_\mathrm{F}}{\partial x} + \frac{E - E_\mathrm{F}}{T}\frac{\partial T}{\partial x}\right] g(E)\, dE\,.\end{aligned} \tag{2.29}$$

With the condition of zero electric current, equations (2.16) and (2.29) give an expression for the thermal conductivity:

$$\begin{aligned}\kappa_\mathrm{e} &= \frac{2}{3m^* T}\left[\frac{\left(\int \tau E^2 \frac{\partial f_0}{\partial E}\, dE\right)^2}{\int \tau E \frac{\partial f_0}{\partial E}\, dE} - \int g\tau E^3 \frac{\partial f_0}{\partial E}\, dE\right] \\ &= \frac{1}{T}\left(K_{r+2} - \frac{K_{r+1}^2}{K_r}\right)\,.\end{aligned} \tag{2.30}$$

The relation of the electrical and the thermal conductivity is described by the *Wiedemann-Franz* law

$$L = \frac{\kappa_\mathrm{e}}{\sigma T}\,. \tag{2.31}$$

With an appropriate L this is a very good approximation for the electronic part of the thermal conductivity. L can be expressed analytically, which reveals values between $L = 2.45 \times 10^{-8}\,\mathrm{W\Omega/K^2}$ for metals and $L = (k_\mathrm{B}/e)^2(r + 5/2)$ for nondegenerate semiconductors.

2.3.5 Seebeck Coefficient

The third important transport property is the thermopower. Due to the Kelvin relations it is sufficient to calculate one of the thermoelectric effects S, Π, τ.[4]

The Seebeck voltage is defined under the condition of zero electric current. Setting equation (2.16) to zero and solving it to $\frac{\partial E_\mathrm{F}}{\partial x}$ yields with equation (2.22) an expression for the Seebeck coefficient:

$$S = \pm \frac{1}{eT}\left(E_\mathrm{F} - \frac{K_{r+1}}{K_r}\right) \tag{2.32}$$

$$= \frac{k_\mathrm{B}}{e}\left(\varepsilon_\mathrm{F} - \frac{r + 5/2}{r + 3/2} \cdot \frac{F_{r+3/2}(\varepsilon_\mathrm{F})}{F_{r+1/2}(\varepsilon_\mathrm{F})}\right)\,. \tag{2.33}$$

2.3.6 Scattering Mechanisms

As pointed out above, the scattering parameter r has a very strong influence on the electronic properties. In most materials there are several mechanisms that contribute to the scattering of the electrons. Most of the important scattering mechanisms can be

[4] The use of τ for the relaxation time and for the Thomson coefficient is somewhat confusing. But it is common symbolic and the Thomson coefficient will appear very rarely in this thesis.

described by a specific scattering parameter. To receive the total scattering parameter, all these contributions must be taken into account using Matthiessen's rule

$$\frac{1}{\tau_{\text{total}}} = \frac{1}{\tau_1} + \frac{1}{\tau_2} + \cdots \tag{2.34}$$

where the τ_i are the individual scattering times.

Acoustic Mode Scattering

Very often scattering by acoustic phonons is the most important scattering mechanism around room temperature. The electrons are scattered by local displacements of lattice atoms due to the lattice vibrations. Bardeen and Shockley originally calculated these effects in [Shockley50] and [Bardeen50]:

$$\mu \propto T^{-3/2} m^{*-5/2} \tag{2.35}$$

$$r = -1/2\,. \tag{2.36}$$

Optical Mode Scattering

In crystals with two or more elements, optical mode vibrations produce an electrical polarization of the lattice which will scatter phonons. Because of the high energy of the optical phonons, these processes can no longer be treated as elastic scattering. Therefore a relaxation time τ does not really exist. Only in the limit of high temperatures the proportionality calculated by Howarth and Sontheimer in [Howarth53] (cited by [Heikes61]) is valid:

$$\tau \propto E^{1/2}\,. \tag{2.37}$$

Neutral Impurity Scattering

At very low temperatures, the excitation of phonon becomes negligible. In this region, scattering by neutral impurities becomes dominant. Erginsoy calculated this mechanism in [Erginsoy50] and obtained

$$\mu \quad \text{independent of } T \tag{2.38}$$

$$r \quad = 0\,. \tag{2.39}$$

This mechanism plays only a minor role in thermoelectric devices, since it is mainly important at very low temperatures.

2.3.7 Heat Conduction — Lattice Part

All the material parameters discussed above are related to the electronic structure of the material and the parameters are correlated to each other in several ways. Therefore, they cannot be optimized independently.

The lattice thermal conductivity is the only parameter in the figure of merit ZT that is not determined by the electronic structure. Therefore it has to be discussed separately.

If an atom in the crystal lattice is thermally excited, the crystal bondings will pass this excitation on to the neighboring atoms. Through this mechanism, heat is transported through the bulk. Because of the periodic structure of the crystal lattice these vibration effects can be described by quasi-particels called *phonons*. These phonons travel through the crystal, carrying a certain amount of energy.

A good approximation for the thermal conductivity for any heat-transporting entity can be derived from the classic kinetic theory:

$$\kappa_\mathrm{l} = \frac{1}{3} C_V l v_\mathrm{s} \tag{2.40}$$

with the specific heat at constant volume C_V and the average velocity of sound v_s and mean free phonon path l.

At very low temperatures the behavior of κ_l is dominated by the Debye T^3 law for C_V. Phonon scattering is insifignicant in this temperature range, because of the low number of excited phonons and their very long wavelength [Wood88, sec. 3.4.1]. At high temperatures, i. e. above the Debye temperature, C_V approaches the classical value of $3R$, making κ_l primarily determined by the behavior of l. (The phonon velocity can be considered almost independent of temperature.)

In a perfect crystal at zero temperature the phonons would move through the crystal uninhibitedly ($l = \infty$), which would result in an infinite thermal conductivity. However, different scattering mechanisms lead to a finite thermal conductivity. The goal in thermoelectric research would be to get a very strong phonon-scattering without affecting the electrical properties.

Phonon–Phonon Scattering

Phonon-phonon scattering is usually the most important scattering mechanism at high temperatures. Two phonons interact with each other, resulting in one phonon. In this process energy is conserved. The wave vector is only conserved to within the first Brillouin zone, following the formulas

$$\hbar\omega_1 + \hbar\omega_2 = \hbar\omega_3 \tag{2.41}$$

$$\mathbf{k}_1 + \mathbf{k}_2 = \mathbf{k}_3 + \mathbf{K} \tag{2.42}$$

where the ω's and $\mathbf{k}$'s are the phonon angular frequencies and the wave vectors, respectively. $\mathbf{K}$ is a reciprocal lattice vector.

The case $\mathbf{K} = 0$ implies conservation of the energy (heat) current. Only collisions with $\mathbf{K} \neq 0$ produce a thermal resistance. Because the flow direction of the phonon is inversed by such a process, it is called an *umklappprozeß*.

In an ideal harmonic lattice, there would be no coupling between the phonon modes. Thus it is the anharmonic part of the lattice potential that causes phonon-phonon collisions.

With this picture in mind, it is easy to understand that the thermal resistance must originate from anharmonic effects in the crystal. Therefore it seems reasonable that it is related to parameters like the thermal expansion coefficient α, the Grüneisen parameter γ or the compressibility χ.

Keyes suggested in [Keyes59] an expression for the lattice thermal conductivity caused by phonon–phonon scattering:

$$\kappa_\mathrm{l} T = \frac{R^{3/2}}{3\gamma^2 \varepsilon^3 N_0^{1/3}} \cdot \frac{T_\mathrm{m}^{3/2} \varrho^{2/3}}{M^{7/6}} \,. \tag{2.43}$$

Here N_0 denotes Avogadro's number, T_m is the melting point and M the mean atomic weight. The dependence of the melting point is introduced by the Lindemann rule that connects the compressibility χ to the melting point, with the help of a constant factor ε.

The first factor in equation (2.43) is almost independent of the material, which allows some conclusions for the thermal conductivity:

- In the high temperature range κ_l follows a 1/T law.
- A low melting point leads to a low thermal conductivity.
- κ_l decreases with increasing atomic mass. This conclusion is not generally true because of the dependence of the parameters of each other. But as Keyes concludes in his paper, the assumption appears to be present in the covalently bonded crystals.
- The proportionality to $\varrho^{2/3}$ makes κ_l low for crystals with large interatomic distances.

Alloy Scattering

In the most state of the art thermoelectric materials alloying is a very successful tool to reduce the thermal conductivity. The idea is to mix two or more materials with the same crystal structure and electron configuration. This should have almost no effect on the electronic properties, but the mass fluctuations cause additional scattering of phonons.

This additional scattering has serveral origins and explanations. The alloyed atoms can be treated as impurities at which the phonons are scattered. The bondings in the crystal are disturbed by the alloying effect, which makes the anharmonic phonon-phonon scattering stronger. Finally, because of the different lattice constants there are strong strain fluctuations in the crystal. These fluctuations can also scatter phonons efficiently. In [Abeles63] some of these effects are treated analytically. He shows that the thermal conductivity is decreased with increasing disorder.

Boundary Scattering

Phonons are scattered at lattice defects, in particular at grain boundaries. Therefore, the lattice thermal conductivity is generally lowered by powdering a material and subsequently pressing it into pellets. However, in most cases the electron mobility is lowered as well. Nevertheless, in some materials the effects on the phonons are stronger than the effects on the mobility. Therefore it is possible to improve the figure of merit of certain materials by this technique [Goldsmid00].

Lower Limit for the Lattice Conductivity

Slack proposed in [Slack79] a lower limit for the lattice thermal conductivity. His calculations are supported by the measurements of Cahill *et al.* in [Cahill92]. The idea is that the mean free path of the phonons cannot be shorter than the wavelength of the phonons. The minimum lattice thermal conductivity is calculated as

$$\kappa_{\mathrm{l,min}} = 3\left(\frac{\pi}{6}\right)^{1/3} k_{\mathrm{B}} \left(\frac{\varrho}{M}\right)^{2/3} v_{\mathrm{s}} \left(\frac{T}{\Theta_{\mathrm{D}}}\right)^{2} \int_0^{\Theta_{\mathrm{D}}/T} \frac{x^3 e^x}{(e^x-1)^2}\, dx\,. \tag{2.44}$$

The velocity of sound is denoted by v_{s}, Θ_{D} is the Debye temperature.[5]

2.4 Guidelines to New Thermoelectric Materials

2.4.1 Charge Carrier Density

By numerical evaluations of the equations for charge carrier density (2.27) and Seebeck coefficient (2.32), it is found that S decreases with increasing charge carrier density. At the same time, σ increases ($\sigma = ne\mu$). To maximize the power factor $S^2\sigma$, the optimum balance between these oppositional effects has to be found. It turns out, that the optimum carrier density is in the range 10^{18} to $10^{20}\,\mathrm{cm}^{-3}$ (see visualization in [Mahan97]).

This is the range of weakly degenerate semiconductors with band gaps up to about $10\,k_{\mathrm{B}}T$ and of semimetals. All of the current state of the art materials fall in this category. To optimize a material, the carrier concentration can be tuned by doping.

2.4.2 Thermal Conductivity

The thermal conductivity consists of two parts: the lattice part and the electronic part ($\kappa = \kappa_{\mathrm{l}} + \kappa_{\mathrm{e}}$). The electronic part is directly connected to the electrical conductivity by the Lorenz number L (see sec. 2.3.4). This results in a limitation of the figure of merit

$$ZT \leq \frac{S^2}{L} = \left(\frac{S}{157\,\mu\mathrm{VK}^{-1}}\right)^2 \tag{2.45}$$

where the equal sign corresponds to $\kappa_{\mathrm{l}} = 0$. To achieve a ZT greater than unity, the thermopower must therefore be at least $157\,\mu\mathrm{V/K}$.

The part of the thermal conductivity that is actually free for manipulations is the lattice part. According to the above mentioned rules, a good candidate for a thermoelectric material should have a complex crystal structure with a high average atomic weight. A low melting point is another sign for a low thermal conductivity. Several systems are attractive because of the ability of alloying. This is a common process to further reduce the thermal conductivity.

[5] With Lindemann's formula, Θ_{D} can be expressed by the parameters used above: $\Theta_{\mathrm{D}} \approx 120\, T_{\mathrm{m}}^{1/2} M^{-5/6} \varrho^{1/3}$.

3 Measurement Techniques

3.1 Electrical Conductivity

The electrical conductivity is a very fundamental transport property. For this work, electrical resistivities are expected in the range from 0.5 mΩcm to 10 Ωcm. This range is easily covered by commercially available measurement systems. In our investigations the Quantum Design 6000 Physical Property Measurement System was used. This automized system allows measurements between 1.7 K and 340 K.

The samples were measured with the four probe technique that eliminates the effect of contact resistances. A typical sample is shown in figure 3.1. The size of the samples was usually about 1 mm × 1 mm × 5 mm.

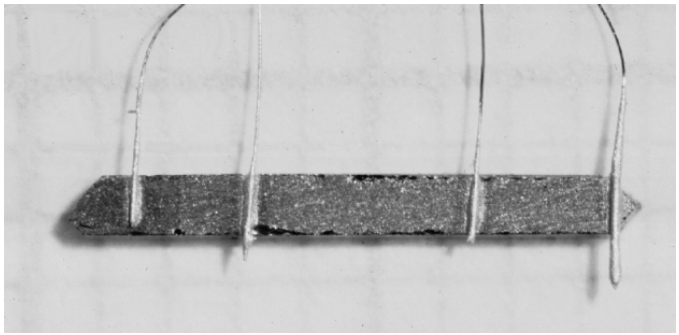

Figure 3.1: Four probe sample for resistance measurement.

Platinum wire was used as leads. It was contacted with silver epoxy. It turned out, that for the Tl_5Te_3 compounds much better contacts could be achieved, if thin gold contacts were evaporated onto the samples, before contacting it with silver epoxy. Gold has a high work function that provides ohmic contact to the *p*-type material.

3.2 Hall Measurements

A four probe technique was also used for the measurements of the hall effect. The sample geometry is shown in figure 3.2. The measurements were carried out in the same Quantum Design system as the resistivity measurements, which provides magnetic fields up to 9 Tesla. Only the range from –1 Tesla to +1 Tesla was used for the measurements. The hall coefficient R_{H} was determined by the slope of a linear regression through several data points at different magnetic fields.

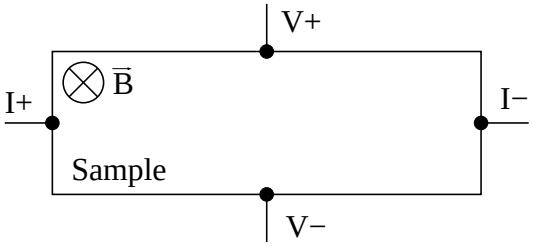

Figure 3.2: Schematic geometry of the hall samples (4 probe measurement).

3.3 Seebeck Coefficient

The Seebeck measurements have been carried out with a self-designed sample holder, that is shown schematically in figure 3.3.

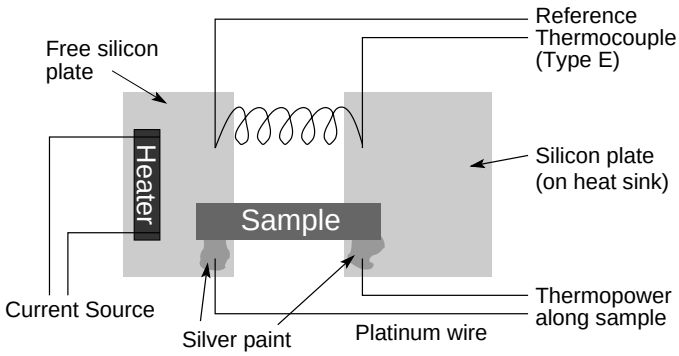

Figure 3.3: Sketch of the setup for the Seebeck measurements.

A sample of approximately 1 mm × 1 mm × 5 mm is mounted onto two silicon plates with silver paint, which also provides the contacts to the leads to a nanovoltmeter. One of the silicon plates is in good thermal contact with a heat sink, while the other silicon plate is only held by the sample. This plate is heated by a resistive heater. The temperature difference is measured by a differential thermocouple, mounted closely to the sample. In all measurements, thermopower was measured with 1.0 and 0.5 Kelvin temperature difference between the plates.

3.4 Thermal Conductivity

The thermal conductivity is a very critical property in the search for good thermoelectrics. Extremely low conductivities are sought for, and at the same time are hard to measure accurately.

Two techniques have been used in this work: a steady-state method and the "3ω method", suggested by [Cahill90]. Wherever possible, the latter method was used. It is less sensitive to radiation losses and can be used for a wide temperature range. However, a sufficiently large homogeneous sample is needed. Therefore, the former method was used for the YNiSb and $Zr_3Ni_3Sb_4$ related compounds.

3.4.1 3ω Method

Radiation losses are an inherent problem in measuring thermal conductivity, in particular with the steady state methods. [Cahill90] therefore describes a different approach, called the 3ω method. This technique allows measurements up to very high temperatures ($\sim 1000\,\mathrm{K}$) with insignificant error from radiation.

This section shall just give an idea of the principle of this technique, and the specific realization in this work. An extensive treatment is given in [Cahill90].

Sample preparation

An area of the sample ($\sim 10\,\mathrm{mm} \times 5\,\mathrm{mm}$) was polished to a very smooth surface, using a fine graded polishing paste. This surface was coated with an electrically insulating glass layer, deposited by spin coating. Finally, a silver or gold line ($\sim 200\,\text{Å}$ thick, $45\,\mu\mathrm{m}$ wide) was evaporated on top through a metal mask. Four pads provided electrical contact to the line for a 4 probe setup. An image of one sample is shown in figure 3.4.

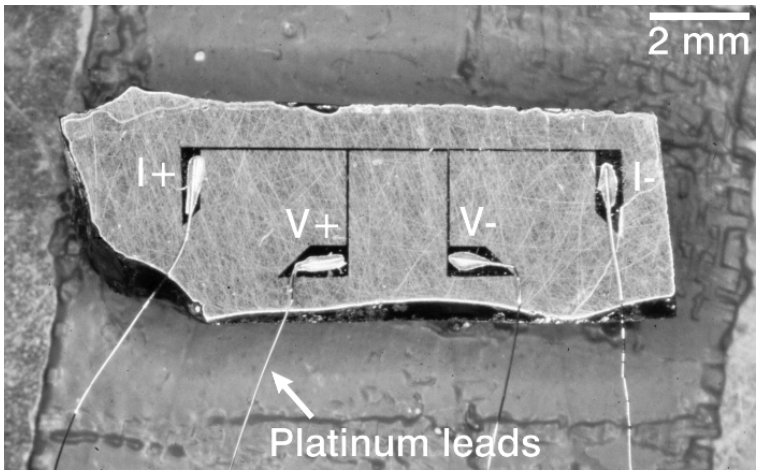

Figure 3.4: Sample for the 3ω technique. The sample is mounted on a heat sink and contacted with platinum wires.

Measurement principle

A current through the silver/gold line, oscillating with angular frequency ω, periodically heats the sample with 2ω.[1] The resistance of the silver/gold line is slightly temperature dependent, resulting in a small resistance oscillation with 2ω. This resistance oscillation (2ω) times the original driving current (ω) result in a small oscillation of the voltage across the line at frequency 3ω.

The heating of the sample is dependent on the thermal conductivity of the underlying sample and on the frequency ω (i. e. the wavelength of the thermal waves propagating into the sample). By measuring the 3ω voltage–frequency dependence, the thermal conductivity of the sample can be calculated. This is treated analytically in [Cahill90]:

$$\kappa = -\frac{V_\omega^3}{4\pi l R^2} \frac{d(\ln f)}{dV_{3\omega}} \frac{dR}{dT} \tag{3.1}$$

where V_ω is the ω voltage, $V_{3\omega}$ the 3ω voltage, R the resistivity of the metal line, $\frac{dR}{dT}$ its derivative by temperature, l is the distance of the two voltage probes, and f is the frequency of the sine voltage.

In the experiments, frequencies between 0.35 and 3.5 Hz were used. This is sufficiently small to neglect the effect of the glass insulation and sufficiently large with respect to the sample geometry. The signals were measured using a Stanford SR830 lock-in amplifier, whose sine generator output was connected to a voltage–current converter to provide a stabilized ω current.

The measurements showed perfect agreement with the theory in [Cahill90], which indicates a very high accuracy.

This technique was used for the Tl_5Te_3 related compounds in this work. Because of their extremely low thermal conductivity, avoiding radiation losses is very critical in these materials. Below 80 K, however, problems emerged because of the different expansion coefficients of the sample and the insulating glass layer and because of the non-linearity of the resistance of the metal line. Therefore, the steady state method was used for very low temperatures.

[1] The induced power is proportional of the square of the current. $\cos^2 \omega \rightsquigarrow \cos 2\omega$.

4

The Tl_5Te_3 Group

The compound Tl_5Te_3 is a known material with the complex B_3Cr_5 structure. Some of its modifications have shown very high thermoelectric performances, in particular Tl_9BiTe_6, which has the highest ZT in the range from 400 to 450 K to date. This success makes the group interesting for deeper investigations.

4.1 Crystal Structure

Bhan and Schubert investigated the crystal structure of Tl_5Te_3 on single crystals [Bhan70]. Their results agree very well with later publications [Schewe89, Villars91, Wolfing00] and show that Tl_5Te_3 crystallizes in space group $I4/mcm$, the B_3Cr_5-type structure.

The unit cell of the B_3Cr_5 structure consists of 32 atoms. The structure is shown in figure 4.1. Two of the four crystallographic sites are occupied by tellurium atoms (Wyckoff sites $4a$ and $8h$), while the thallium atoms are on the $4c$ and $16l$ sites.

4.2 The Ternary Modifications of Tl_5Te_3

The thallium atoms on the $4c$ sites can partly or fully be replaced by other elements, resulting in two groups of ternary compounds: Tl_4XTe_3 (X: Sn or Pb) and Tl_9XTe_6 (X: Sb or Bi).

The formation of these compounds can be understood by a look at the valence states of Tl_5Te_3. As a member of the chalcogenide group, tellurium can be assumed to be in the valence state Te^{2-}. To provide 6 electrons, the 5 thallium atoms must have different valence states.

Nordell and Miller propose in [Nordell96] the valence state Tl^{1+} for the $16l$ atoms and Tl^{2+} for the $4c$ site. This assignment is based on a comparison of bond distances, the coordination environments and Mulliken populations with other thallium compounds. The formula Tl_5Te_3 can thus be rewritten as $Tl_4^{1+}Tl^{2+}Te_3$.

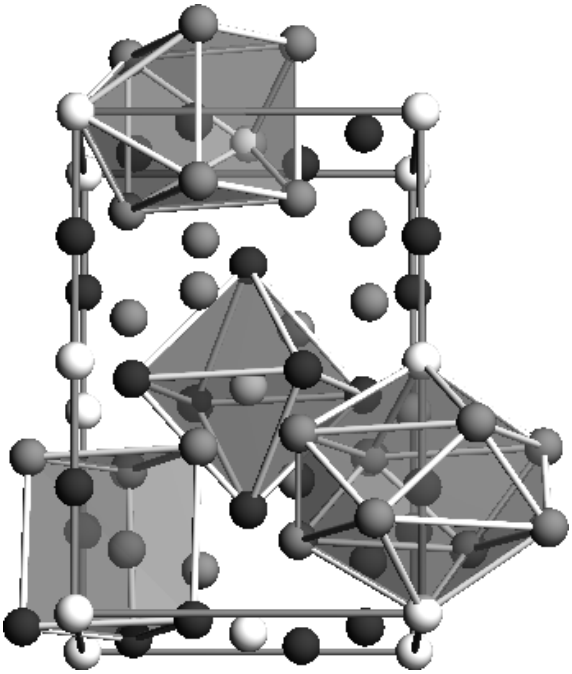

Figure 4.1: Structure of the compounds in the Tl_5Te_3 group. The unit cell consists of 32 atoms on 4 different sites. The indicated polyhedra are the corresponding coordination polyhedra. Tellurium atoms are shown in dark gray, thallium atoms in white for the 16*l* site and in light gray for the 4*c* site.

4.2.1 The Modifications $Tl_8Sn_2Te_6$ and $Tl_8Pb_2Te_6$

By substituting the Tl^{2+} atoms by another bivalent element, the Tl_4XTe_3 compounds are formed. The most interesting representatives of this group are for thermoelectric applications: $Tl_8Sn_2Te_6$ and $Tl_8Pb_2Te_6$. For the latter the corresponding selenide $Tl_8Pb_2Se_6$ exists as well [Houenou81].

4.2.2 The Modifications Tl_9BiTe_6 and Tl_9SbTe_6

The electron configuration of thallium, $[Xe]4f^{14}5d^{10}6s^26p^1$ suggests the valence states Tl^{1+} and Tl^{3+} rather than the bivalent state Tl^{2+}. And indeed, as Nordell points out in [Nordell96, sec. 3.2], Tl^{2+} easily disproportionates into Tl^{1+} and Tl^{3+}. So another way to write the formula Tl_5Te_3 is $Tl_9^{1+}Tl^{3+}Te_6$, where the unit formula has been expanded to obtain integral atom numbers. In this view, the 4*c* site of the Tl_5Te_3 crystal is equally occupied by Tl^{1+} and Tl^{3+}.

By substituting the Tl^{3+} with the trivalent atoms Sb or Bi, the second group of ternary compounds is formed: Tl_9SbTe_6 and Tl_9BiTe_6. Again, the corresponding selenides, Tl_9SbSe_6 and Tl_9BiSe_6, exist as well [Barchii88].

Tl_9BiTe_6 has been extensively investigated in [Wolfing00]. It has been proven to be a highly efficient thermoelectric material. An extensive investigation of the whole group, including its alloys, might therefore lead to even higher efficiencies.

4.3 Known Thermoelectric Properties

4.3.1 Electrical Properties

Earlier publications by Latypov and Pradel [Latypov88, Pradel82] reported rather poor thermoelectric properties of the Tl_5Te_3-related compounds. They measured thermopowers up to $80\,\mu V/K$ and resistivities of about $2\,m\Omega cm$.[1] For Tl_9BiTe_6, Pradel reported a thermopower of $62\,\mu V/K$ and a resistivity of $1.5\,m\Omega cm$. With a thermal conductivity of $0.7\,W/Km$ this lead to a figure of merit of $ZT = 0.1$ at $300\,K$.

Compared to these results, dramatic improvements have been achieved recently [Wolfing00]. Purification of the elements prior and of the ternary compounds after the reaction substantially enhanced the Seebeck coefficient of these compounds with only a small loss of electrical conductivity.

Wölfing found the most efficient material in the Tl_5Te_3 family to be Tl_9BiTe_6. Here, a Seebeck coefficient of $261\,\mu V/K$ was measured with a resistivity of $6.7\,m\Omega cm$. The resulting powerfactor of about $1 \times 10^{-3}\,W/K^2m$ is more than three times smaller than for Bi_2Te_3, but due to its extremely low thermal conductivity, Tl_9BiTe_6 outperforms pure Bi_2Te_3 at room temperature and above.

The compound Tl_9BiSe_6 was found to have a much higher Seebeck coefficient of $700\,\mu V/K$ at room temperature. But this increase in the thermopower is accompanied by an increase of the resistivity by almost five orders of magnitude to roughly $150\,\Omega cm$, which results in a very poor powerfactor of about $3 \times 10^{-7}\,W/K^2m$ (compared to $1 \times 10^{-3}\,W/K^2m$ for Tl_9BiTe_6).

4.4 Possible Improvements in this Group

Among the seven ternary compounds in the Tl_5Te_3 group, Tl_9BiTe_6 has already been identified as the compound with the best thermoelectric properties. Any search for thermoelectric materials in the Tl_5Te_3 group should therefore be closely related to this material.

A common technique in optimizing thermoelectric materials is the formation of alloys of iso-electronic materials. As explained in section 2.3.7, this should lower the thermal conductivity while leaving the electronic properties unchanged.

[Wolfing00] studied the alloying effects in the Tl_9BiTe_6–Tl_9BiSe_6 system. This did not lead to a higher thermoelectric performance. Tl_9BiSe_6 has a very high electrical resistivity that strongly reduces the power factor. Even with small additions of Tl_9BiSe_6, the power factor became too low to make this material interesting.

The compound Tl_9SbTe_6 is the material that is closest to Tl_9BiTe_6 in the Tl_5Te_3 family. Its electronic properties are not too far away from the Tl_9BiTe_6 compound. The dramatic drop in the power factor by alloying is therefore not expected for Tl_9SbTe_6–Tl_9BiTe_6 alloys. In the following chapter, Tl_9SbTe_6 is characterized in detail to form a basis for the studies on the alloys. In chapter 6, the whole Tl_9SbTe_6–Tl_9BiTe_6 system is investigated.

No experiments have been made yet to tune the charge carrier density by doping Tl_9BiTe_6. [Wolfing00] developed cleaning techniques to achieve Tl_9BiTe_6 with a very

[1] In [Latypov88] no temperature is given, but it is very likely that the data were taken at room temperature.

high purity. This forms the starting point to investigate doping effects on Tl_9BiTe_6.

Depending on the dopants also *n*-type material can be obtained, which is necessary to build a thermoelectric device based solely on Tl_9BiTe_6, since for a thermoelectric device both types of thermoelectrics are needed. However, not all compounds exhibit the same thermoelectric performance for *p*- and *n*-type material.

Both aspects of doping are studied in chapter 7. *n*-type Tl_9BiTe_6 turns out to be not as efficient as its *p*-type counterpart. By *p*-type doping, however, some improvements could be achieved.

5 The Compound Tl_9SbTe_6

In the Tl_5Te_3 group Tl_9SbTe_6 is the closest neighbor to Tl_9BiTe_6. This makes it a good starting point for further studies in the group. In this chapter the pure Tl_9SbTe_6 is characterized. The data of this chapter will be the basis for the measurements on Tl_9BiTe_6–Tl_9SbTe_6 alloys, which will be discussed in the next chapter.

5.1 Sample Preparation

As Wölfing pointed out in his work, purity has an important impact on the transport properties of the Tl_5Te_3 compounds. This impact was also observed on Tl_9SbTe_6. For the investigations in Tl_9SbTe_6 and its alloys with Tl_9BiTe_6, only zone refined materials were used.

The samples were synthesized from the elements as described in [Wolfing00, chp. 7.1]. Purification was done by zone refining, also described in [Wolfing00]. The material looked clean and shiny, x-ray diffraction showed no impurities or other phases.

5.2 Electronic Properties

The resistivity of Tl_9SbTe_6 is significantly lower than that of Tl_9BiTe_6. In figure 5.1 the resistivity data is compared to a $T^{3/2}$ curve, which is expected for acoustic phonon scattering. The good agreement indicates that this scattering mechanism is dominant over a wide temperature range.

The main reason for this increased conductivity is a higher carrier concentration. Hall measurements show a concentration in the order of $10^{20}\,cm^{-3}$ that is only slightly increasing with temperature. This carrier concentration is about one order of magnitude higher, compared to Tl_9BiTe_6. Because of the lower mobility at room temperature ($27\,cm^2/Vs$ for Tl_9SbTe_6 vs. $62\,cm^2/Vs$ for Tl_9BiTe_6), the electrical conductivity only increases by a factor of about five.

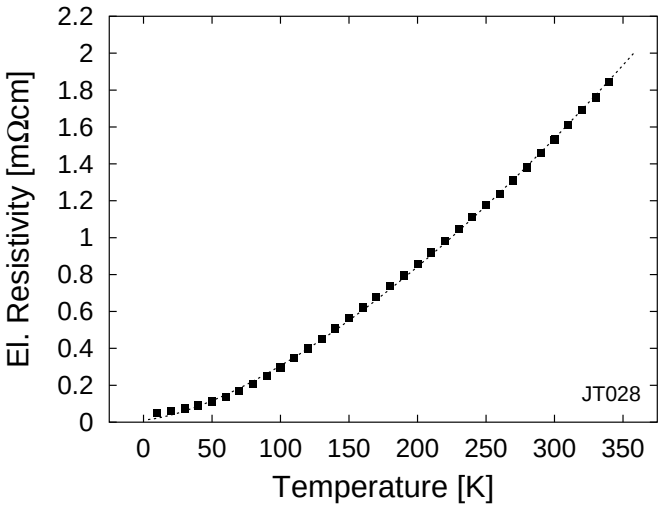

Figure 5.1: Electrical resistivity of zone refined Tl_9SbTe_6. The dotted line is a $T^{3/2}$ fit for temperatures above 50 K to show that acoustic phonon scattering is the dominant scattering mechanism.

As in Tl_9BiTe_6, the temperature dependence of the mobility is mainly determined by two scattering mechanisms: neutral impurity scattering at low temperatures and acoustic phonon scattering in the high temperature range. For their determination, hall measurements have been carried out with the results shown in figures 5.2(a) and 5.2(b).

To calculate the mobility from the hall measurements, a weighted hall factor r_H was used in figure 5.2(a), as described in [Wolfing00, sec. 6.4.2]. The hall factor r_H is varied over temperature between 1 (neutral imp.) and 1.18 (acoustic phonon). This gives a slightly better estimation of the low temperature part, compared to using a value of 1.18 over the whole temperature range.

Compared to Wölfing's data on Tl_9BiTe_6, the mobility is about five times higher in the low temperature part. The contribution by neutral impurity scattering is calculated to 1500 cm^2/Vs, which is about twice as high as in Tl_9BiTe_6. This indicates a very high purity in the sample.

5.3 Magnetic Properties

A high mobility makes the material interesting for magnetical measurements. Detailed measurements at different temperatures have been carried out to observe magnetoresistivity. This effect describes the dependence of the electrical resistivity on the quadratic of the magnetic field. It gives another way to determine the mobility.

The magnetoresistivity follows the formula [Seeger99, sec. 4.4]

$$\frac{\Delta\varrho}{\varrho(B)} = \frac{\varrho(B) - \varrho_0}{\varrho(B)} = T_M(\mu B)^2 \tag{5.1}$$

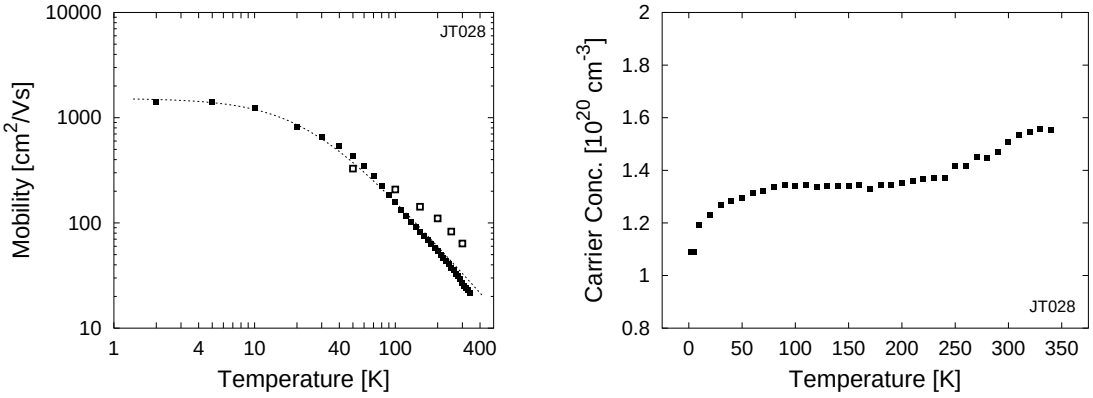

(a) Mobility of Tl_9SbTe_6

(b) Carrier concentration of Tl_9SbTe_6

Figure 5.2: Hall measurements on zone refined Tl_9SbTe_6. The mobility is dominated by two scattering mechanisms: neutral impurity (dominant for low temperatures, const.) and acoustic mode scattering (high temperatures, $\propto T^{-3/2}$). The empty squares in figure 5.2(a) have been determined from the magnetoresistivity. The carrier concentration is about one order of magnitude higher than the concentration in Tl_9BiTe_6.

where the factor T_M depends on the scattering parameter r by

$$T_M = \frac{9\pi}{16} \frac{(3r+\frac{3}{2})!(r+\frac{3}{2})! - [(2r+\frac{3}{2})!]^2}{[(r+\frac{3}{2})!]^4} . \tag{5.2}$$

The numerical value of T_M varies between 0.38 (for $r = -\frac{1}{2}$, acoustic mode scattering) and 2.15 (for $r = \frac{3}{2}$, inonized impurity scattering).

Assuming only acoustic mode scattering as an active mechanism,[1] this allows to calculate the carrier mobility independently from the hall measurements. The results are in reasonable agreement with the hall measurements. The datapoints are drawn in as empty squares in figure 5.2(a).

5.4 Seebeck Effect

As discussed in section 2.4.1, the increased carrier density comes along with a lower Seebeck coefficient. As in Tl_9BiTe_6, the thermopower — shown in figure 5.3 — grows linearly with increasing temperature over the investigated temperature range to 340 K.

If the linear behavior of the high temperature region is extrapolated to lower temperatures, a sign change of the Seebeck coefficient would be expected at about 70 K. A sign change, however, cannot be observed, S stays positive over the whole temperature range. This indicates that the Seebeck coefficient is partly compensated, which lowers its value by about 40 μV/K. If this compensation could be suppressed, a higher Seebeck coefficient is expected.

With 100 μV/K at room temperature, Tl_9SbTe_6 has less than half the thermopower of Tl_9BiTe_6. This thermopower is too low to use the pure Tl_9SbTe_6 compound as a

[1] For $r = 0$, T_M becomes zero. Neutral impurity only becomes important at very low temperatures.

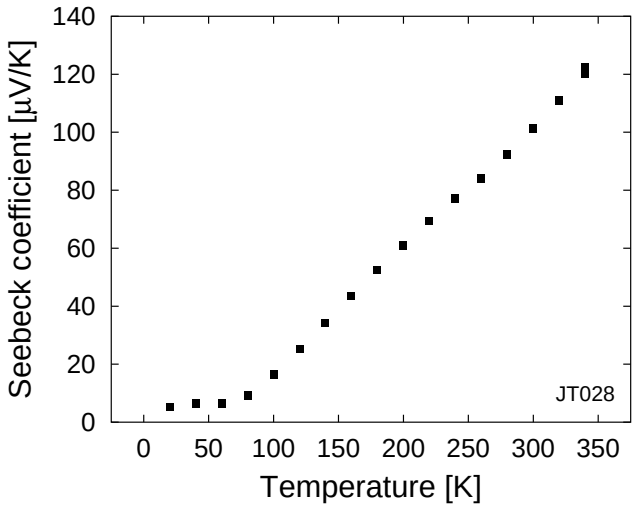

Figure 5.3: Seebeck coefficient of zone refined Tl_9SbTe_6.

thermoelectric material. But as the material is fully miscible with Tl_9BiTe_6, Tl_9SbTe_6 opens some possibilities to tune the properties of Tl_9BiTe_6 by properly alloying the two compounds.

5.5 Thermal Conductivity

The key to the outstanding performance of Tl_9BiTe_6 is its extremely low thermal conductivity. It even outperformes one of its neighbors in the Tl_5Te_3 group, $Tl_8Pb_2Te_6$, by a factor of 2. The thermal conductivity of Tl_9SbTe_6 is therefore a very important property in the search for optimized thermoelectric materials.

In figure 5.4, the thermal conductivity of Tl_9SbTe_6 is compared to Tl_9BiTe_6. The total conductivity (denoted by squares) is the measured value, while the lattice part has been calculated by subtracting the electronic part, according to the Wiedemann-Franz law (with the Lorenz number for metals, $L = 2.45 \times 10^{-8}\,\mathrm{W\Omega/K^2}$, see page 11).[2]

Two oppositional effects can be expected, when replacing the bismuth in Tl_9BiTe_6 by antimony, and it is not a priori clear, which mechanism is the dominant one:

- Tl_9SbTe_6 has a lower average atom mass. With Keyes' formula (see equation (2.43) on page 14) this should lead to a *higher* lattice thermal conductivity.
- The antimony atoms in Tl_9SbTe_6 have a larger mass difference to the thallium atoms on the same ($4c$) lattice site, compared to the bismuth in Tl_9BiTe_6. As mentioned in section 2.3.7, mass fluctuations act as scattering centers that *lower* the lattice conductivity.

The experiment shows that it is the latter effect, that dominates the thermal conductivity of Tl_9SbTe_6. For low temperatures the lattice conductivity is even significantly

[2] This Lorenz number is valid for a highly degenerate electron gas. With carrier concentrations in the order of $10^{20}\,\mathrm{cm^{-3}}$ this approximation seems justified.

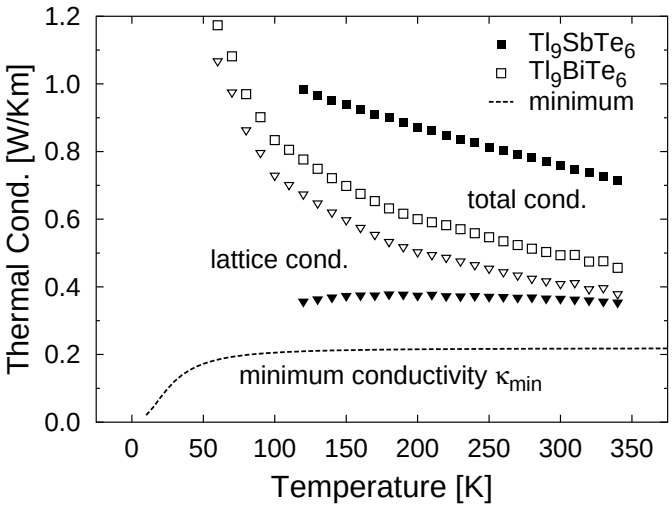

Figure 5.4: Thermal conductivity of Tl_9SbTe_6 in comparison to Tl_9BiTe_6. The total conductivity is denoted with squares, the lattice part with triangles. Data points for Tl_9SbTe_6 are filled, those for Tl_9BiTe_6 empty. The dashed line shows the minimum lattice thermal conductivity, according to Slack's formula (see section 2.3.7).

lower than in Tl_9BiTe_6, while for room temperature and above, both compounds have an almost equal lattice conductivity.

This conclusion is not only supported by the absolute value of κ_l, but also by its temperature dependence. In contrast to Tl_9BiTe_6, the lattice thermal conductivity of Tl_9SbTe_6 does not follow a T^{-1} law, but stays almost constant over the whole measurement range. The T^{-x} law for Tl_9BiTe_6 indicates phonon-phonon scattering as the dominating mechanism.

In a simplified theory for ideal crystals, a T^{-1} law is predicted for phonon-phonon scattering. Because of an increasing phonon number with raising temperature, the free phonon path decreases as T^{-1}. With an almost constant C_V, the thermal conductivity follows the T^{-1} law, too (see equation 2.40 on page 13).

In a non-perfect material, however, exponents can be expected between $x = 0$ and $x = 3$ — depending on the contribution of different phonon scattering mechanisms [Berman79, sec. 8.2.1]. Defect scattering should make a temperature independent contribution ($x = 0$). This temperature indepencence is seen in the thermal conducitivity of Tl_9SbTe_6, which corresponds well with its low absolute value.

The importance of disorder effects on the 4*c* site in the Tl_5Te_3 structure was already pointed out in [Wolfing00, sec. 9.2.1] where Tl_9BiTe_6 showed a significantly lower thermal conductivity than $Tl_8Pb_2Te_6$. In $Tl_8Pb_2Te_6$, the 4*c* is completely occupied by Pb atoms, while in Tl_9BiTe_6 this place is equally occupied by thallium and bismuth (see also the crystal structure on page 22).

In Tl_9SbTe_6 this disorder is even stronger than in Tl_9BiTe_6 and the lattice thermal conductivity comes close to its lower limit, explained in section 2.3.7. The calculated κ_{min} is shown in figure 5.4 for comparison. It has been calculated with a Debye tem-

perature of 124 K, which is the value for Tl_9BiTe_6, given in [Wolfing00]. The Debye temperature can be estimated with Lindemann's formula [Ziman60], using the melting point, the mean atomic weight, and the atomic distances of the unit cell. As all these quantities are almost equal in both compounds, the same Debye temperature can be assumed.

5.6 Summary

With a thermoelectric figure of merit of 0.27 at room temperature Tl_9SbTe_6 is a very efficient thermoelectric material. Although it cannot compete with its neighbor Tl_9BiTe_6, it is still a very interesting material on its own. Both compounds are very closely related members of the Tl_5Te_3 group. This is reflected in their thermoelectric properties that show very similar behavior. Tl_9SbTe_6 has a very high electrical conductivity (five times higher than Tl_9BiTe_6.), but the lower Seebeck coefficient leads to a performance that is about 40 % lower than that of Tl_9BiTe_6. The figure of merit ZT is shown in figure 5.5.

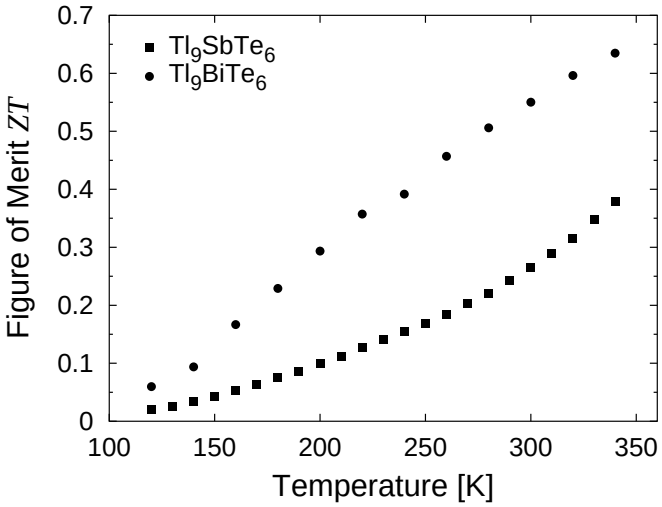

Figure 5.5: The figure of merit ZT for Tl_9SbTe_6, compared to Tl_9BiTe_6. Tl_9SbTe_6 stays about 40 % behind Tl_9BiTe_6, due to its lower thermopower. Both compounds are very good thermoelectric materials.

The outstanding feature of the Tl_5Te_3 related compounds is the extremely low thermal conductivity. Regarding the lattice conductivity, Tl_9SbTe_6 shows even lower values than Tl_9BiTe_6. The total value, however, is higher, because of the large electronic part.

As both compounds show very good thermoelectric performance, the formation of solid solutions between the two materials seems very promising. The alloy system Tl_9SbTe_6–Tl_9BiTe_6 is therefore investigated in the next chapter. Particular attention is paid to the thermal conductivity that is expected to drop by alloying.

6

The Alloy System Tl_9SbTe_6–Tl_9BiTe_6

The compound Tl_9BiTe_6 has proven to be a very efficient thermoelectric material, mainly because of its low thermal conductivity. The related compound Tl_9SbTe_6 has shown an even lower lattice thermal conductivity, but falls back in the electronic properties.

By the formation of solid solutions between those two materials, the optimum balance is sought for. As phonon scattering by disorder on the Tl/Bi (Tl/Sb) site has played an important role in both materials, solid solutions may be expected to have an even lower thermal conductivity, caused by additional alloy scattering.

6.1 Sample Preparation

Purity and synthesis process of the Tl_5Te_3 related compounds have shown to have a strong impact on the thermoelectric performance (see e. g. [Wolfing00, chp. 6.4]). To rule out any influence of the preparation process, "master" compounds have been formed. These master compounds have been prepared from purified elements and zone refined after the preparation. This purification technique has shown a significant performance improvement for all Tl_5Te_3 related compounds and is described in [Wolfing00, chp. 8.4]. All subsequent samples were prepared by mixing the master compounds according to the desired composition and remelting them in a tube furnace.

This approach is much easier to handle, because the ternary compounds can be processed under air. It also rules out any non-stochiometry effects, as the stochiometries are locked to those of the master compounds.

The non-isotropic expansion coefficient very often lead to little cracks and holes when the melted ingots were cooled down. This makes the material hard to handle, and makes transport measurements less reliable. The number of cracks has been reduced by using the directional freezing of the material in the zone refining furnace. In order to prevent unintentional re-separation of the base substances, only one refinig step was made and no signs of phase separation have been observed in any of the samples.

6.2 X-Ray Diffraction

X-ray diffraction experiments have been carried out with several different compositions of $Tl_9Bi_xSb_{1-x}Te_6$. They did not only show the variation of the lattice constants, but also prove the miscibility of the system. All samples appeared to be phase pure and completely miscible.

With the smaller atom diameter of antimony, the lattice constants of Tl_9SbTe_6 are slightly smaller compared to Tl_9BiTe_6. But unlike in the Tl_9BiTe_6–Tl_9BiSe_6 system the lattice constants follow "Vegard's law". According to this rule in [Vegard21] the lattice spacings in solid solutions should vary linearly between the spacings of the end members. The results of the x-ray measurements are shown in figure 6.1, where linear fits have been drawn in as guides to the eye.

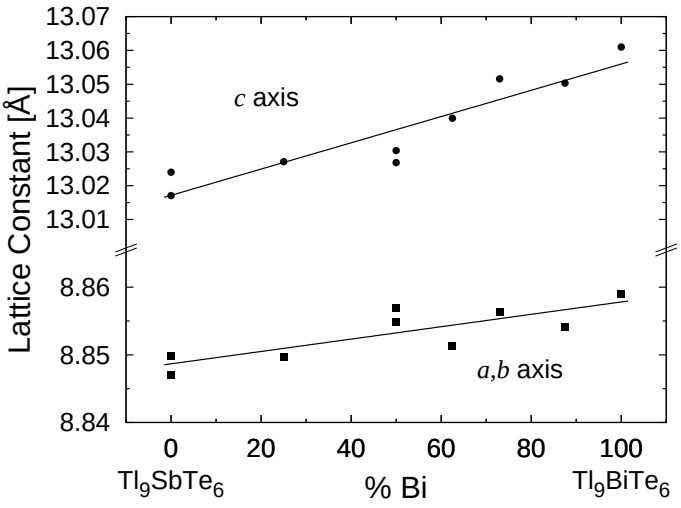

Figure 6.1: The alloying effect on the lattice constants is very small and in the range of the resolution of the x-ray spectrometer (note the different scales for both plots).

An interesting property of the Tl_5Te_3 compounds was observed during the measurements: The material appeared to be sensitive to pressure. After powdering the materials in a mortar, the lattice constant of the powder was clearly lowered. In order to minimize this effect, all samples where annealed in a sealed quartz ampoule after powdering.

6.3 Electronic Properties

As the two end points of the alloy system, Tl_9BiTe_6 and Tl_9SbTe_6, have already been investigated, the analytical expressions from chapter 2 can be used to estimate the thermoelectric performance of the alloys. All compounds are highly degenerated semiconductors — far away from the simplified system regarded in the theory chapter, which assumes single parabolic bands. So it is not surprising that those estimations only agree with the measurements to a limited extent.

The numerical calculations are presented in this section and then compared to the observed values in the next section. In all calculations the room temperature behavior, i. e. at 300 K, was regarded.

6.3.1 Seebeck Coefficient

The Seebeck coefficient has been measured to 101 μV/K for Tl_9SbTe_6 and 281 μV/K for Tl_9BiTe_6. With equation (2.32) the corresponding Fermi energies can be determined. This leads to energies of 62 meV and –29 meV for Tl_9SbTe_6 and Tl_9BiTe_6, respectively.[1] A scattering parameter of $r = -\frac{1}{2}$ was assumed for these calculations, as both compounds showed acoustic phonon scattering as the dominant electron scattering mechanism.

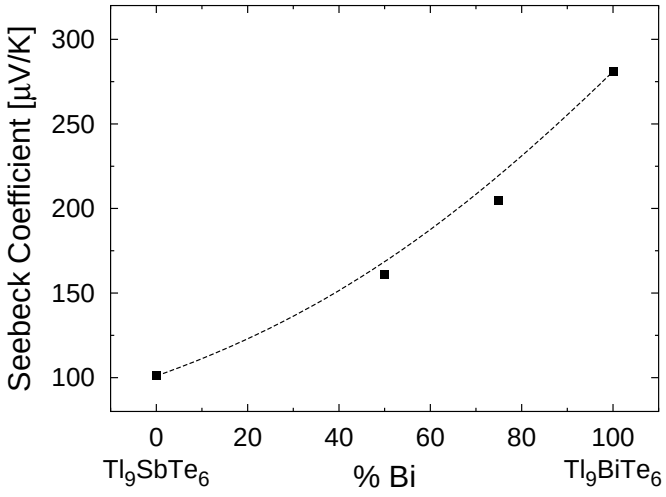

Figure 6.2: The Seebeck coefficient in the Tl_9SbTe_6–Tl_9BiTe_6 alloy system. Measurements are denoted by squares. The line is a calculated curve, based on a linear variation of the Fermi energy between the ends of the system. The calculation has been fixed to the two end points (see text).

For the further calculations a linear variation of the Fermi energy between the two end values has been assumed. The predicted behavior of the thermopower (shown as a line in figure 6.2) agrees quite well with the measured values, which are only slightly lower than predicted.

[1] The Fermi energy is measured from the conduction band edge. If it is negative, the Fermi level is pushed into the band gap and the Seebeck coefficient increases. Positive values are in the conduction band and the thermopower is decreased. In contrast to [Wolfing00, chp. 7.3] zone refined material was used. This lead to a different Fermi energy of Tl_9BiTe_6.

6.3.2 Charge Carrier Density

As derived in section 2.3.3, the carrier concentration of a semiconductor with single parabolic bands is given by

$$n = 2\left(\frac{m^* k_\mathrm{B} T}{2\pi\hbar^2}\right)^{3/2} F_{1/2}(\varepsilon_\mathrm{F})\,. \tag{6.1}$$

With a given Fermi energy the effective density-of-states mass can be determined from hall measurements. With a measured carrier concentration of $1.5 \times 10^{20}\,\mathrm{cm}^{-3}$ an effective mass of $1.6\,m_e$ is obtained for Tl_9SbTe_6. The carrier concentration of Tl_9BiTe_6 is $1.2 \times 10^{19}\,\mathrm{cm}^{-3}$, which results in an effective mass of $1.5\,m_e$. Both values are very close to each other and are reasonable in value.

The effective mass is a parameter to describe the band structure. The almost equal value for both compounds indicates a very similar band structure, at least in the region close to the energy gap — the most important region for a thermoelectric material.

6.3.3 Electrical Conductivity

In section 2.3.2 an analytical expression was derived for the electrical conductivity:

$$\sigma = \frac{8^{3/2} e^2 \tau_0 \pi m^{*1/2}}{h^3} (k_\mathrm{B} T)^{r+3/2} \left(r + \frac{3}{2}\right) F_{r+1/2}(\varepsilon_\mathrm{F})\,. \tag{6.2}$$

To describe the conductivity of a material, another parameter is needed, in addition to the Fermi energy and the effective mass. The factor of proportionality τ_0 in equation (6.2) (or equation (2.11), respectively) describes the scattering time of the electron scattering process, in this case the electron–phonon scattering. For Tl_9BiTe_6 this factor is 1.5 times larger than for Tl_9SbTe_6. Electron scattering is therefore stronger in Tl_9SbTe_6 than in Tl_9BiTe_6.

The ionic radius of antimony is smaller than the one of bismuth and thallium. This leads to stronger strains in the lattice that enhance electron–phonon scattering, i. e. lowers the scattering time, expressed by τ_0.

To estimate the resistivity for the alloy system, a linear variation of τ_0 within the alloy composition was used. Fermi energy and effective mass have also been varied linearly between the end values. The resulting resistivity is shown in figure 6.3. The curvature here is stronger than for the Seebeck coefficient.

6.3.4 Power Factor — Summary of the Electronic Properties

Three approximations have been made to describe the Tl_9SbTe_6–Tl_9BiTe_6 alloy system:

- The Fermi energy E_F varies linearly in the alloy system, between 62 meV for Tl_9SbTe_6 and –29 meV for Tl_9BiTe_6.
- The effective masses m^* of both end compounds are almost equal. Its value is also varied linearly between $1.6\,m_e$ for Tl_9SbTe_6 and $1.5\,m_e$ for Tl_9BiTe_6.
- The scattering time constant τ_0 is approx. 1.5 times larger for Tl_9BiTe_6 than for Tl_9SbTe_6. It is also assumed to vary linearly in the alloy system.

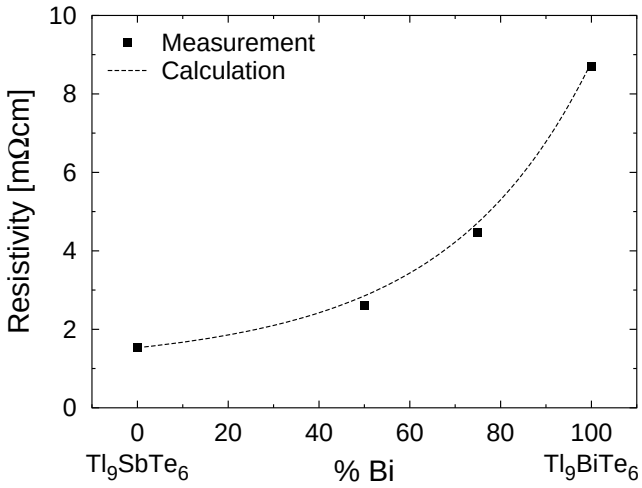

Figure 6.3: Resistivity measurements in the Tl_9SbTe_6–Tl_9BiTe_6 alloy system. The line is calculated with the same Fermi energies as in figure 6.2 and a linear variation of the factor τ_0 with the alloy composition.

With these assumptions, an estimated power factor can be calculated for the alloy system. The result is shown in figure 6.4.

For the alloy composition with about 70 % Tl_9BiTe_6 a maximum of the power factor is expected. This maximum power factor exceeds the power factor of pure Tl_9BiTe_6 by about 15 %. If these estimations can be validated by actual measurements, Tl_9SbTe_6–Tl_9BiTe_6 alloys might exceed the thermoelectric performance of pure Tl_9BiTe_6. An expected lower thermal conductivity due to alloy scattering would further enhance this performance.

For the thermal conductivity, the alloy effect is expected to be most efficient in the middle of the alloy system, as maximum disorder is achieved in that case. But the minimum in the lattice conductivity is expected to be very broad and a significant drop is already expected close to the end components. So the preparation of materials closer to the Tl_9BiTe_6 end seems to be most promising.

6.4 Measurements

Seebeck, resistivity, and hall measurements have been carried out on compounds of the alloy system. The Seebeck and resistivity data of the samples is shown in figures 6.5. All samples show the same temperature dependence and a clear trend in the variation of the alloy composition. Both quantities raise monotonic with increasing bismuth content.

At high temperatures the mobility follows for all samples the $T^{-3/2}$ law (acoustic phonon scattering), with an increasing mobility from $27\,cm^2/Vs$ for Tl_9SbTe_6 to $62\,cm^2/Vs$ for the Tl_9BiTe_6 end (300 K). The carrier concentration is almost temperature independent for all samples and varies between $1.5 \times 10^{20}\,cm^{-3}$ for Tl_9SbTe_6 and $1.2 \times 10^{19}\,cm^{-3}$ for Tl_9BiTe_6 (room temperature values).

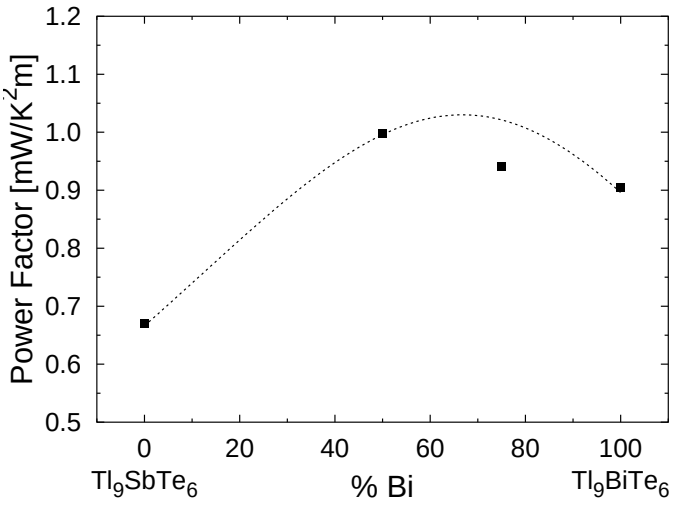

Figure 6.4: Theoretical estimation of the power factor in the alloy system. For an alloy composition with about 70 % bismuth a maximum is expected.

With these results the measurements follow almost exactly the calculated values. The values have been drawn in in the above figures of the calculations. In the two graphs with Seebeck coefficient and resistivity, the measured values are only slightly below the expectations. The same agreement was observed in the mobilities and carrier concentrations.

Considering the fact that the calculations were only based on very simple approximations, this agreement is quite surprising. The analytical expressions were derived for a nondegenerate semiconductor with single parabolic bands. The three parameters Fermi energy, effective mass, and τ_0 were obtained by a simple linear interpolation. In a complex system like the $Tl_9Sb_xBi_{1-x}Te_6$ system, these approximations cannot generally assumed to be true.

The maximum in the power factor is not as pronounced in the measurements as expected from the calculations. Only the sample with 75 % Tl_9BiTe_6 contribution does not exactly follow the predicted curve. The reason for this is its slightly lower thermopower. As the power factor is proportional to the quadratic of the Seebeck coefficient, this lower value strongly impacts the power factor. However, all samples with a high bismuth contribution show high power factors. The alloy process indeed kept the good electronic performance of the end compounds.

6.5 Thermal Conductivity

Aside from optimizing the electronic properties, i. e. the power factor, another important aspect to investigate in the Tl_9SbTe_6–Tl_9BiTe_6 alloy system is the possible reduction of the thermal conductivity by alloy scattering. This mechanism to reduce the lattice part of the thermal conductivity is described in sec. 2.3.7 and has been a very successful step in the improvement of many thermoelectric materials.

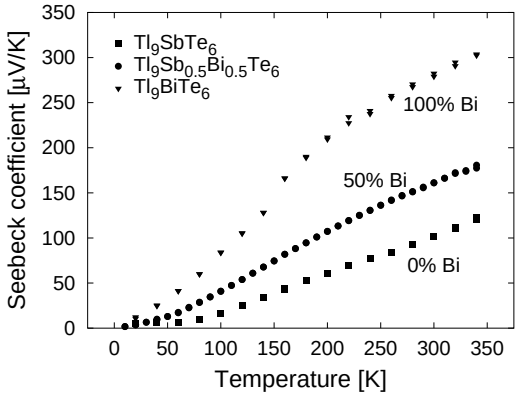

(a) Seebeck coefficient in the alloy system

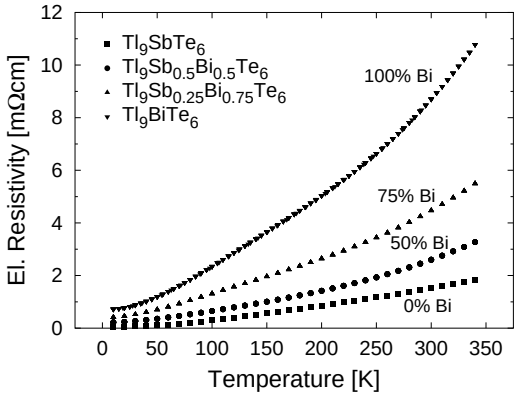

(b) Resistivity in the alloy system

Figure 6.5: Seebeck coefficient and resisitivity in the Tl_9SbTe_6–Tl_9BiTe_6 alloy system. Due to their similar electronic structure, all samples show the same temperature dependence. Both quantities raise monotonic with increasing bismuth content.

6.5.1 Measurement

Thermal conductivity measurements have been carried out with the 3ω method from 340 K to 80 K. For lower temperatures, our setup could not be used, because of the different expansion coefficients of the sample and the isolating glass layer, that destroyed the samples for lower temperatures. Tl_9SbTe_6 could not be measured below 120 K. For Tl_9SbTe_6 and the 50:50 compound a gold line was used instead of the silver line described in section 3.4.1. The use of gold allows measurements to higher temperatures, up to about 450 Kelvin.

With the use of silver, the contact over the thin line broke at elevated temperatures. The reason for this might be a chemical reaction of the silver with the surrounding air. Measurements above 340 K have been carried out in a tube furnace under a lower vacuum of about 10^{-2} to 10^{-3} Torr. The use of gold as an alternative eliminated that problem.

For the gold line, a parasitic annealing effect was observed. That changed the electrical resistivity of the gold line if the line was annealed at high temperatures. The temperature dependence of the resistivity of the gold line is a very critical parameter in the determination of the thermal conductivity of the sample. To rule out any annealing effects during the measurements, the gold line was annealed for several hours slightly above the highest measured temperature. After this annealing process the resistivity of the line showed the typical linear temperature dependence of a metal. No further annealing during the measurements was observed.

6.5.2 Thermal Conductivity

Lower Temperature Region

Figure 6.6 compares the lattice parts of the thermal conductivity of four samples in the low temperature region. The electronic part has been subtracted with the use of the

Wiedemann-Franz law. Tl_9BiTe_6 shows the known T^{-1} behavior, the conductivity of Tl_9SbTe_6 stays almost constant over the whole temperature range as already described in section 5.5.

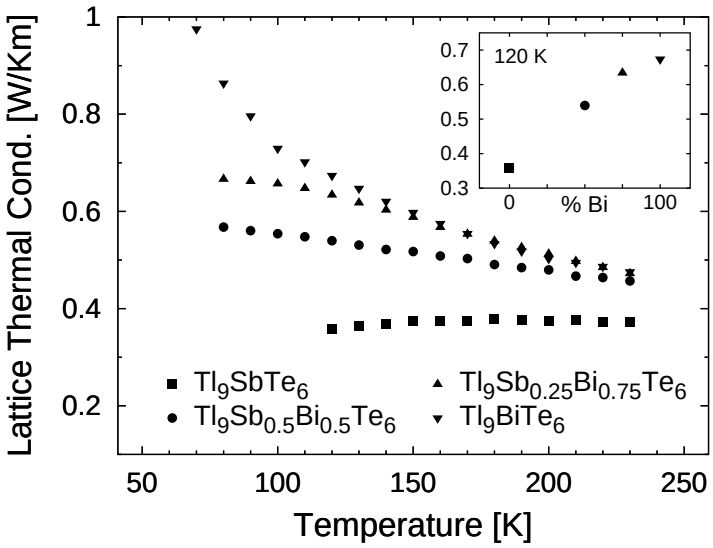

Figure 6.6: Lattice thermal conductivity versus temperature of some compounds in the Tl_9SbTe_6–Tl_9BiTe_6 alloy system. The inset shows the almost linear dependence on the alloy composition at 120 Kelvin.

The lattice conductivity of the mixed compounds, however, varies almost linearly between the ends of the alloy system. An additional reduction of the thermal conductivity by alloy scattering could not be observed. The variation of the thermal conductivity with the alloy composition is shown in the inset of figure 6.6 for a temperature of 120 K.

The Tl and the Bi/Sb atoms are equally distributed over the 4*c* lattice sites. The mass fluctuations on this site efficiently scatter phonons and reduce the thermal conductivity. The mass fluctuations between the thallium atoms and the bismuth/antimony atoms appear to be most important for this scattering process. Fluctuations between bismuth and antimony have a minor effect on phonon scattering.

Room Temperature and Above

It was already stated in section 5.5, that the lattice thermal conductivities of Tl_9BiTe_6 and Tl_9SbTe_6 are almost equal at room temperature and above. The absolute values vary around 0.4 W/Km. As the lattice conductivity can only be determined indirectly from the total conductivity and the electrical resistivity, these small variations are within the error range.

The reduction that was seen for lower temperatures almost vanishes for temperatures above 250 K. This is consistent with the reports of [Callaway60], where the disorder in ^{6}LiF and ^{7}LiF solid solutions is analytically treated as point imperfections. The scattering effect of these imperfections is significantly stronger for low temperatures and almost vanishes for higher temperatures.

The higher temperature region is dominated by phonon–phonon scattering, that does not significantly change within the alloy system. In particular, no alloy scattering was observed.

To determine the thermoelectric figure of merit, the total thermal conductivity of the material is important. With an almost constant lattice part, the variation of the total conductivity within the alloy system is determined by the electrical conductivity. The total thermal conductivity therefore varies linearly between the end compounds. A linear interpolation between the end compounds has been made to estimate the thermoelectric performance of the alloy system in the next section.

6.6 Conclusions

To see the improvement potential by alloying in Tl_9BiTe_6, estimations of the power factor have been made, using a simplified theory to describe the system. A maximum of the power factor was predicted for a composition with about 70 % Tl_9BiTe_6 contribution (shown again in figure 6.7). These calculations were confirmed by measurements on different samples of the alloy system, although the maximum was not as pronounced as suggested by the calculations.

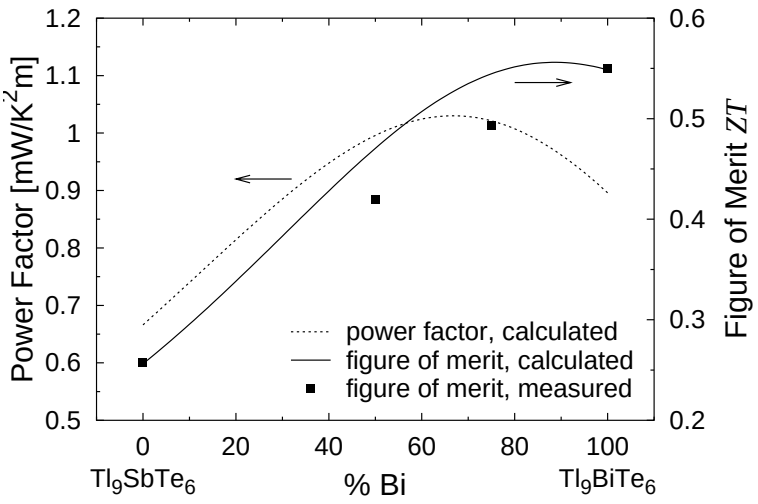

Figure 6.7: Thermoelectric performance of the Tl_9SbTe_6–Tl_9BiTe_6 alloy system. The solid line is the calculated figure of merit ZT, using the power factor from section 6.3.4 (drawn in as a dotted line) and a linear interpolation of the measured thermal conductivities. The squares are the actually measured ZT.

For low temperatures the lattice thermal conductivity of Tl_9SbTe_6 is lower than the one of Tl_9BiTe_6. In the alloy system this lattice component varies almost linearly between the end compounds for low temperatures. An additional reduction by alloy scattering cannot be observed. Because of a higher electronic part, however, the total thermal conductivity is higher in Tl_9SbTe_6 over a very large temperature range.

At room temperature and above it is mainly this electronic part of the thermal

conductivity that determines the variation of the total conductivity with the alloy composition. It causes a linear shift of the total thermal conductivity between the end compounds. The lattice contribution stays constant in the whole alloy system. No additional alloy scattering can be observed.

With its significantly lower electronic part, the thermal conductivity of Tl_9BiTe_6 is lower compared to Tl_9SbTe_6. To estimate the figure of merit ZT for the whole temperature range, the power factor from section 6.3.4 was divided by a linear interpolation of the thermal conductivity between the end compounds, and multiplied by the corresponding temperature, 300 K. The result is shown in figure 6.7 as a solid line.

The variation of the thermal conductivity compensates the maximum of the power factor. Instead of forming a maximum, the dimensionless figure of merit flattens out at the Tl_9BiTe_6 end. Following these calculated values, no improvement of the thermoelectric performance can be obtained by alloying in the Tl_9SbTe_6–Tl_9BiTe_6 system.

The actual measurements (shown in figure 6.7 as squares) even show a monotonic, almost linear, increase of ZT towards the Tl_9BiTe_6 end. It can be concluded that Tl_9BiTe_6 is the best thermoelectric material in this alloy system.

7 Doping of Tl_9BiTe_6

As already pointed out in chapter 2, there is an optimum region of the charge carrier density to maximize the power factor $S^2\sigma$. This region usually is at about 10^{18} to $10^{20}\,cm^{-3}$ (see e. g. [Mahan97]).

The charge carrier concentrations can be varied by appropriately doping the material. In order to distinguish the effects of intentional doping from impurity effects, very pure material is needed as a starting point. Different purification methods for Tl_9BiTe_6 have been studied extensively [Wolfing00]. Based on these results, the possibilties of improving Tl_9BiTe_6 by appropriate doping have been studied.

Another important aspect for thermoelectric applications is the availability of both types of materials: *p*-type and *n*-type. As synthesized and after zone refining Tl_9BiTe_6 always appears as *p*-type material. In order to produce *n*-type material, doping with the group V elements Sb and Bi was investigated.

7.1 Sample Preparation

For the preparation process two important aspects have to be taken into account:

- The base elements of Tl_9BiTe_6, as well as the doping material mercury, are very difficult to handle, because of their reactivity and toxicity.
- All materials should be kept as clean as possible and the impurity level should be the same in all samples.

7.1.1 Doping in Melt

Because of these two points, preparation of the doped samples from the elements is not feasible. Instead, the dopant was added to zone refined Tl_9BiTe_6 and then sealed in an evacuated quarz ampoule. The ampoule was then melted at 650 °C for several hours to get the doped sample.

Because of the non-isotropic expansion coefficient of Tl_9BiTe_6, the produced ingots mostly had little cracks or holes that would result in inaccurate transport measurements. Therefore, the samples have been frozen in the temperature gradient of the zone refining furnace. The dircetional freezing resulted in solid ingots without cracks. Because a purification of the sample was not aimed for in this stage, the speed of the ampoule transport in the furnace was set to about 3 to 4 times the normal speed and only one or two passes were made.

7.1.2 Doping by Evaporation

A way to keep the materials as clean as possible in the doping process is doping by evaporation and in-diffusion. The dopant is evaporated on a thin piece of Tl_9BiTe_6 (In this work, sometimes readily prepared rods for the various transport measurements have been used.). The sample is then sealed in a quartz ampoule and heated up to about 400 °C. This temperature supports the diffusion of the dopant into the sample, while staying well below the melting point of the material.

This technique gives good control over very low doping levels. The doping depends on the thicknesses of the sample and the evaporated dopant. And the technique requires less material than the doping in melt.

On the other hand, this technique is only suitable for low doping levels. The homogenity of the dopant distribution in the sample depends on the diffusion coefficient of the system. But after diffusion times of 1 – 2 weeks the diffusion length $\sqrt{D_0 t}$ should exceed the sample thickness of ~ 1 mm, if a diffusion coefficient D_0 in the order of the typical values for metals is assumed [Weast84]. To avoid effects of remaining dopants on the surface, a small layer was polished off after the annealing process.

In the first doping experiments with bismuth, the bismuth formed several small isles on the surface of the sample. This was because of the low melting point of bismuth (271 °C), and apparently bismuth does not wet Tl_9BiTe_6. In further experiments all the bismuth doped samples were heated to 200 °C to start the diffusion process with the solid bismuth phase. After two days the temperature was raised to 400 °C and no isles or droplets of bismuth have been observed.

7.2 n-Doping with Sb and Bi

After the success with Tl_9BiTe_6 as a *p*-type thermoelectric material, the question arises, if Tl_9BiTe_6 can also be efficiently doped to act as the *n*-type arm of a thermoelectric device. B. Wölfing showed in [Wolfing00, chp. 7.4] that it is indeed possible to get *n*-type material in the Tl_5Te_3 group. He successfully doped Tl_9BiSe_6 with bismuth, resulting in a negative Seebeck coefficient.

7.2.1 The Effect of Bi Doping

Figure 7.1(a) shows the behavior of a Tl_9BiTe_6 sample that has been moderately doped with Bi in melt (0.1 formula unit Bi added to Tl_9BiTe_6).

For low temperatures the material shows a *p*-type behavior with a Seebeck coefficient that is even higher than the one of pure Tl_9BiTe_6. At about 90 Kelvin, the Seebeck voltage drops and changes to a negative value as high as –600 μV/K at 200 K.

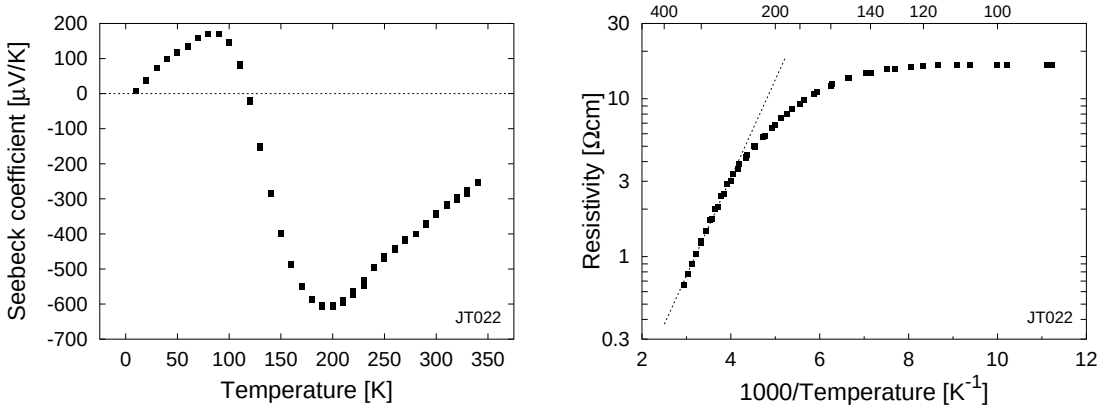

(a) Seebeck coefficient of Bi doped Tl_9BiTe_6

(b) Resistivity of Bi doped Tl_9BiTe_6

Figure 7.1: Seebeck coefficient and resisitivity of Bi doped Tl_9BiTe_6. The sample shows *p*-type behavior for low temperature and a high *n*-type Seebeck coefficient for temperatures above 120 K. The logarithmic plot of the resistivity versus reciprocal temperature shows an activated behavior with an activation energy of 250 meV.

This shows that it is indeed possible to make *n*-type Tl_9BiTe_6. In order to explain the changing sign of the thermopower, resistivity and hall measurements have been carried out.

The resistivity, shown in figure 7.1(b), exhibits an activated behavior and it is about one order of magnitude higher than the resistivity of undoped Tl_9BiTe_6.

The slope of the high temperature part in figure 7.1(b) gives an estimation of the activation energy of the semiconductor. The dotted line corresponds to an activation energy of 246 meV. This value corresponds well with an estimation from the Seebeck measurements. Following [Goldsmid99], the band gap can be estimated to

$$E_g \cong 2eS_{max}T_{max} \tag{7.1}$$

where S_{max} is the maximum Seebeck coefficient and T_{max} is the temperature at which this maximum is reached. For the second maximum at 200 K ($S_{max} = -600\,\mu V/K$) this equation yields a value of 240 meV.

The idea behind equation (7.1) is that for low temperatures the Seebeck coefficient is dominated by extrinsic charge carriers, and S rises with temperature as the Fermi energy moves away from the band edge. For higher temperatures, electron-hole pairs are excited across the band gap and S is reduced because of the opposing effect of the two types of charge carriers.

The Seebeck coefficient in figure 7.1(b), however, shows two maxima. A second maximum with a positive thermopower of about 170 μV/K is observed at a temperature of 85 K. With equation (7.1) this corresponds to an activation energy of $\sim$30 meV. This indicates the formation of another impurity level.

The formation of more than one energy level by the dopant is also indicated by the hall coefficient R_H, which shows an untypical behavior. At low temperatures, R_H is positive. Then, at about 190 Kelvin, it turns negative and becomes positive again at

about 230 Kelvin. This behavior must be related to the mechanisms that determine the Seebeck coefficient. The temperature dependence of both quantities corresponds fairly well, as shown in figure 7.2(a), where the three transport properties have been appropriately scaled and drawn into one graph.

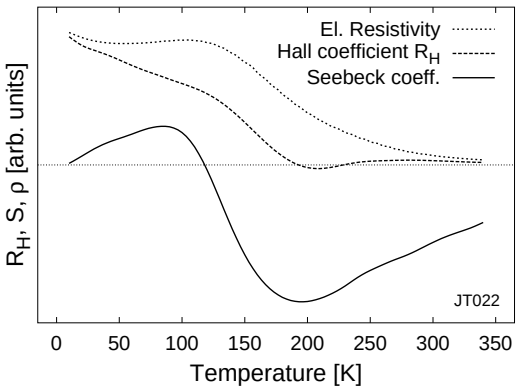

(a) Hall coefficient R_{H}, Seebeck coefficient S, and resistivity ϱ of Bi doped Tl_9BiTe_6

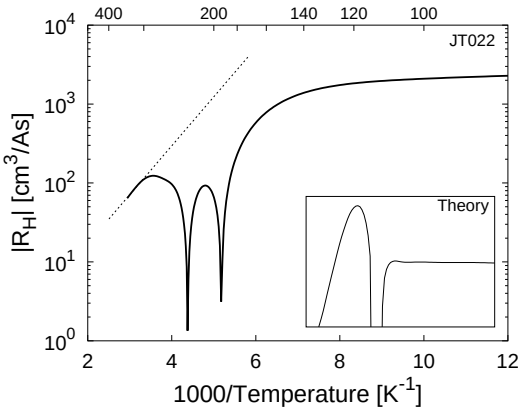

(b) Hall coefficient R_{H} versus reciprocal temperature

Figure 7.2: The three transport parameters R_{H}, S, and ϱ in comparison. In agreement with the theory, all parameters show the same trends.
The right plot shows the Hall coefficient R_{H} versus reciprocal temperature. For a semiconductor with two types of charge carriers a behavior as shown in the inset is expected [Seeger99, chp. 4.3]. The dotted line is solely based on the activation energy calculated in figure 7.1(b).

As described in [Seeger99, chp. 4.3], the hall coefficient can change its sign if more than one type of charge carriers is present. A curve as in the inset of fig. 7.2(b) is expected in the case of one dopant. Bi doped Tl_9BiTe_6 almost follows this theoretical curve, including the high temperature part, that should tend to a line as indicated in the plot. The slope of this line was only calculated on the basis of the activation energy determined by the resistivity data.

7.2.2 Dependence on the Doping Level

The above described features slowly envolve with increasing Bi doping level. This can be seen in figure 7.3, where samples with different Bi additions are compared.

With increasing Bi doping level, two maxima evolve. The Seebeck coefficient in these maxima becomes considerably higher than the one of pure Tl_9BiTe_6. Compensation and recombination of holes leads to a lower charge carrier density in this regions that makes the thermoelectric voltage increase.

At higher doping levels, the high temperature peak of the Seebeck coefficient flips over to a negative value because the electrons now overcompensate the holes. If the doping level is further raised, the Seebeck coefficient has an almost linear behavior. The material is now completely n-type. And while all the other doped samples were

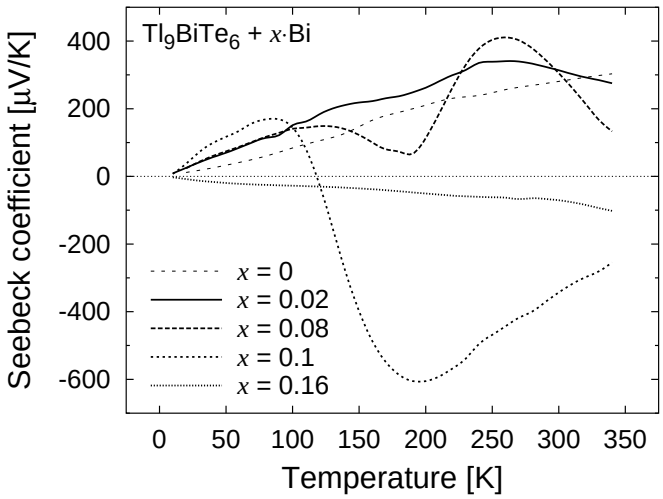

Figure 7.3: Dependence of the Seebeck coefficient on the doping level. Samples with different bismuth additions are compared to purified Tl_9BiTe_6.

semiconducting, the high doped material has an almost constant resistivity over a large temperature range.

7.2.3 Conclusions

The foregoing sections showed that it is indeed possible to synthesize n-type Tl_9BiTe_6. However, the temperature dependence of the Seebeck coefficient already shows that n-type Tl_9BiTe_6 is a partly compensated material with more than one type of charge carriers. This makes it very unlikely to get a high performance material by n-type doping.

A look on the resistivity shows that the power factors of this material stay far behind the ones of p-type material. All Bi doped samples have been semiconducting with activation energies in the range of 250 – 300 meV. Room temperature values and low temperature values are listed in table 7.1

dop. level x	ϱ at 10 K [Ωcm]	ϱ at 10 K [Ωcm]
0.0	0.0007	0.009
0.02	5.6	0.18
0.08	18.6	1.4
0.1	17.4	1.2
0.16	0.19	0.17

Table 7.1: Resistivities of different Bi doped samples (Tl_9BiTe_6 +x·Bi) at 10 Kelvin and 300 Kelvin.

7.2.4 Doping with Sb

Antimony has the same electron configuration as bismuth, and the Tl_9SbTe_6 compound also exists in the Tl_5Te_3 group. Therefore doping experiments with antimony have been carried out. The effect of antimony doping is not as significant as the bismuth equivalent. *n*-type material could not be achieved by Sb doping.

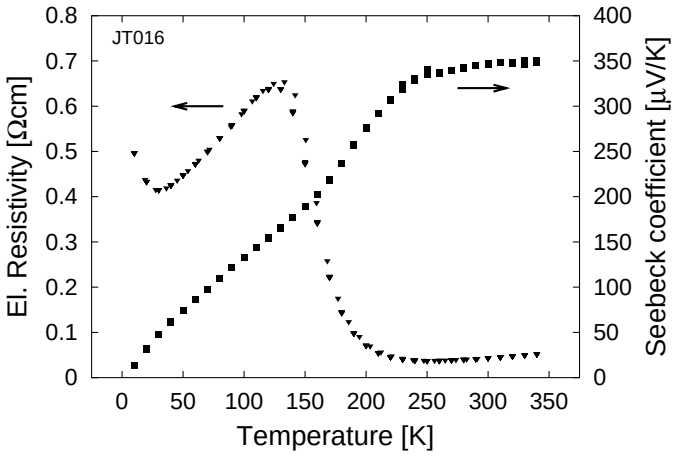

Figure 7.4: Seebeck coefficient for Sb doped Tl_9BiTe_6. Although the Seebeck coefficient is enlarged by the Sb doping, the power factor is a factor of 3 lower than of pure Tl_9BiTe_6, due to the high resistivity.

Instead the Seebeck coefficient increased from 280 μV/K (pure Tl_9BiTe_6) to 346 μV/K after adding some antimony. However, at the same time the material became semiconducting with a room temperature resistivity of about 43 mΩcm, which is roughly five times the resistivity of pure Tl_9BiTe_6. In the power factor this resulted in a reduction by a factor of about 3.

Antimony seems therefore not to be an interesting dopant for Tl_9BiTe_6, neither to achieve *n*-type material, nor to improve the *p*-type properties of Tl_9BiTe_6.

7.3 p-Doping with HgTe

The "classical" way of doping is to partly replace the element on one crystal site with one of its immediate neighbors in the periodic table of the elements. The direction of the movement in the periodic table thereby defines the effect of the dopant: the element to the right acts as a donator, the element to the left as an acceptor.

In Tl_9BiTe_6 *p*-type doping should be possible by substituting thallium with mercury. Mercury, however, is very toxic and hard to handle. An alternative to doping with pure mercury is the use of HgTe. HgTe is solid and stable on air, which makes it much easier to handle. Tellurium is a constituent of the base material Tl_9BiTe_6 and is expected to act as a *p*-type dopant, too.

7.3.1 Sample Preparation

Several samples with different dopant concentrations have been prepared by adding HgTe to Tl_9BiTe_6 in the melt. Annealing for a few hours in this liquid state at 650 °C leads to sufficient mixing of the dopant with the material.

It turned out that the non-isotropic expansion coefficient of Tl_9BiTe_6 made much more problems than with the samples in the previous chapters. Cooling the sample down to room temperature produced large holes in all samples. With the use of the directional freezing in the zone refining furnace, the number of these holes could be significantly reduced. But even after a slow cooling process over 24 hours the samples stayed very brittle. This made the transport measurements very problematic.

The reason for these problems could not be explained. The same problems appeared with all samples, but all of them were phase pure, according to x-ray powder diffraction measurements. The powder spectrum of one sample is shown in figure 7.5 and exactly matches the spectrum calculated for pure Tl_9BiTe_6.

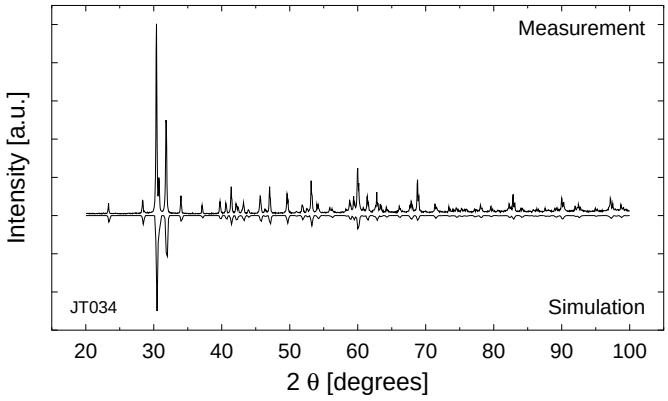

Figure 7.5: X-ray diffraction pattern of Tl_9BiTe_6, doped with HgTe. For comparison a simulated pattern for pure Tl_9BiTe_6 is shown.

7.3.2 Electrical Conductivity

The above mentioned problems were reflected in the resistivity measurements. Many samples showed high resistivities that increased, when the sample was cooled down to 10 K and heated up again to room temperature. This indicates the formation or enlargement of little cracks in the material, that increase the electrical resistivity.

The variations between the measured values of different samples were dominated by these processes, rather than by the doping effects. Tiny cracks have a significant impact on the resistivity of the sample. But they can only lead to an increase of the electrical resistivity. The measured value is therefore an upper limit to the actual resistivity, which means a lower bound to the thermoelectric performance.

The best thermoelectric performance was measured on a sample with the composition $Tl_9BiTe_6 + (HgTe)_{0.16}$. After processing the sample in the zone refining furnace, this sample had no visible cracks. This was confirmed by the resistivity measurements,

which reproduced the same values as the material was cooled down and heated up again. The results of the measurements are shown in figure 7.6, where the resistivity of pure Tl_9BiTe_6 has been drawn in for comparison.

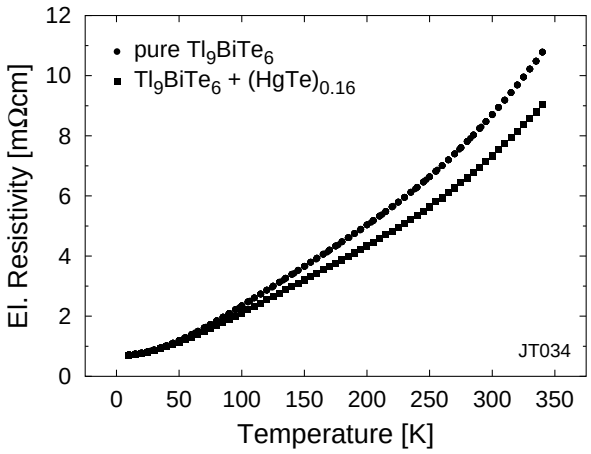

Figure 7.6: Resistivity of p-doped Tl_9BiTe_6, in comparison to purified Tl_9BiTe_6. After addition of 0.16 formula units HgTe the electrical resistivity dropped by about 20 %.

As expected from p-type doping, the addition of HgTe reduced the electrical resistivity by about 20 %. The reason for that is an increased number of charge carriers. Hall measurements revealed carrier densities around $2.6 \times 10^{19}\,\mathrm{cm}^{-3}$, that do not significantly change with temperature. This is more than twice the number of charge carriers than in zone refined Tl_9BiTe_6 ($1.2 \times 10^{19}\,\mathrm{cm}^{-3}$). This increase, however, is accompa-

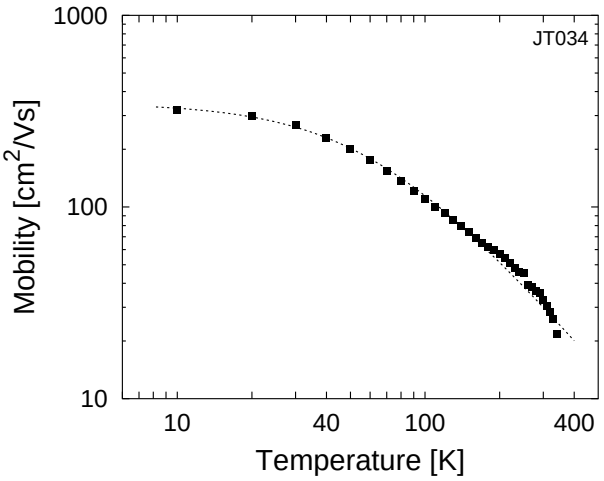

Figure 7.7: Hall mobility of HgTe-doped Tl_9BiTe_6. Neutral impurity scattering is important in the low temperature region, while for high temperatures acoustic phonon scattering becomes dominant.

nied by a decrease in the mobility from 62 cm^2/Vs to 32 cm^2/Vs (see figure 7.7), which results in a net increase of the electrical conductivity by about 20 %.

The temperature dependence of the mobility is similar to the dependence in pure Tl_9BiTe_6. The low temperature part is dominated by neutral impurity scattering, that leads to a temperature independent contribution. For higher temperatures, the mobility follows a $T^{-3/2}$ law, which is expected for acoustic phonon scattering.

7.3.3 Seebeck Coefficient

While the homogenity of the sample has a strong impact on its electrical resistance, the little cracks have almost no influence on the measurement of the Seebeck coefficient. All samples showed thermopowers very similar to the one of pure Tl_9BiTe_6.

On the same sample that was used for the above resistivity measurements Seebeck measurements were carried out. Doping has no significant effect on the thermopower. In figure 7.8 both materials are compared. In conjunction with the increased electrical conductivity, the power factor was enhanced by about 20 %. Doping with HgTe started to impact the Seebeck coefficient only for rather high doping levels. After the addition of 0.45 formula units HgTe the thermopower decreased to 200 μV/K.

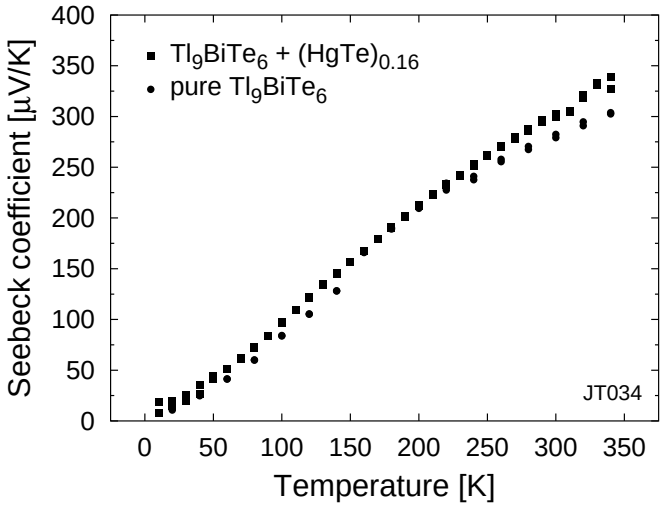

Figure 7.8: Seebeck coefficient of HgTe-doped Tl_9BiTe_6, compared to pure Tl_9BiTe_6. The thermopower stays almost unaffected by the dopant.

7.3.4 Conclusions

Doping effects have been investigated by p-doping Tl_9BiTe_6 with HgTe. The measurements indicated improvements of the thermoelectric power factor $S^2\sigma$ by up to 20 %. Compared to pure Tl_9BiTe_6 the maximum of the power factor was observed for slightly higher temperatures. Both materials are compared in figure 7.9.

But with the HgTe-doping the material became extremely brittle. This prevents the material from being used in an actual device. However, the study shows that

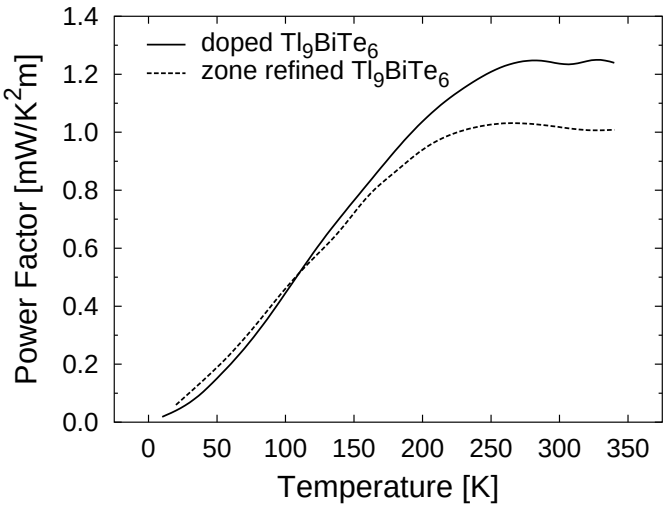

Figure 7.9: Power factor of HgTe-doped Tl_9BiTe_6 in comparison to zone refined Tl_9BiTe_6. Doping increased the power factor by about 20 % at room temperature.

an improvement of the thermoelectric performance is possible by *p*-doping Tl_9BiTe_6. To circumvent the mechanical problems, further studies are necessary. With modified preparation techniques or new dopants a significant improvement of Tl_9BiTe_6 is very promising.

8 The YNiSb Group

The Half-Heusler-Phases form a large group of intermetallic compounds. Some of these compounds exhibit a semiconducting or semimetallic behavior with small band gaps. In conjunction with the fairly complex unit cell, the materials became more and more attractive for thermoelectric applications in the recent years. The many iso-electronic compositions open a lot of possibilities to fine-tune these materials and optimize their thermoelectric properties.

In the recent years, the compounds MNiSn (M = Ti, Zr, Hf) gained a lot of interest in the search for thermoelectric materials, after a figure of merit $ZT \approx 0.41$ was reported for the compound $Zr_{0.5}Hf_{0.5}NiSn$ in [Hohl97].

[Larson99] and [Sportouch99] suggested the group MNiPn (M = Y, La, Yb, and Lu, X = Sb, As, and Bi) for thermoelectric applications. Their band structure calculations predicted a semiconducting behavior with band gaps in the range 0.1 – 0.5 eV.

Several materials of this group have been synthesized and evaluated regarding their thermoelectric properties. Brief studies have been carried out to investigate the possibilities of optimizing the materials by alloying and/or doping.

8.1 Crystal Structure

The Heusler- and Half-Heusler-Phases are well-known intermetallic compounds since many years. Heusler-Phases are represented by a cubic lattice with the general formula M'_2MX, where M and M' are metals, and X is an metalloid or metal.

If the M' place is only half occupied, the Half-Heusler-Phase M'MX is formed. It is also known as "half-stuffed rocksalt" or MgAgAs structure. The structure is depicted in figure 8.1.

Starting with YNiSb, all the three crystal sites can be substituted by iso-electronic atoms. Yttrium can be replaced by scandium, luthetium or other rare-earth metals, nickel by palladium or platinum, and antimony by bismuth or arsenic. All the combinations exist and most of the compounds should exhibit semiconducting behavior.

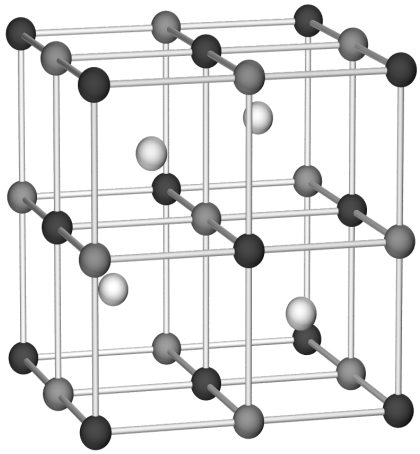

Figure 8.1: The crystal structure of YNiSb. Yttrium atoms are black, antimony dark grey. Y and Sb form a NaCl-type lattice with eight spaces. In YNiSb, four of them are occupied by nickel atoms, the other four stay empty.

This behavior is predicted by band structure calculations [Larson99]. It can also be deducted from the "Grimm-Sommerfeld" rule [Bucher99].

As all these phases are known to exist and have the same electron configuration, it is expected, that all solid solutions between the members of this group exist as well. This feature is not only interesting for the optimization as a thermoelectric material by lowering the thermal conductivity and optimizing the electronic properties, it also opens a large field to investigate the effects of alloying from a research point of view.

8.2 Sample Preparation

All the investigated materials have very high melting points, above 1100 °C. This leaves only few possibilities to synthesize the samples. In this work, two preparation methods were used: arc melting and solid-state reaction in a sealed quartz ampoule.

8.2.1 Arc Melting

Stochiometric mixtures of the elements were melted together in an arc furnace under argon atmosphere. The congelted ingot was turned over and remelted several times to ensure a homogeneous sample. The sample was then annealed at 900 °C for several days.

Synthesis by arc melting resulted in easy to handle, homogeneous ingots. However, a major drawback is the possible loss of volatile elements during the process. Therefore, precise control over the stochiometry can only be ensured with a lot of effort.

As antimony has the highest vapor pressure among the three components[1], it is most likely to volatilize. By adding some additional antimony, the loss can partly be compensated. A way to minimize the losses is the use of pre-melted binaries. For most of the samples used in this work, YNi has been pre-melted, or the respective binary in the other compounds.

X-ray powder diffraction shows that the material had completely reacted and a one-phase material had been formed. The patterns agreed with the known patterns of

[1] The vapor pressure of antimony or bismuth is about 6 to 8 orders of magnitude larger than the one of yttrium or nickel.

Half-Heusler compounds. As an example, the pattern of an arc melted sample is shown in figure 8.2.

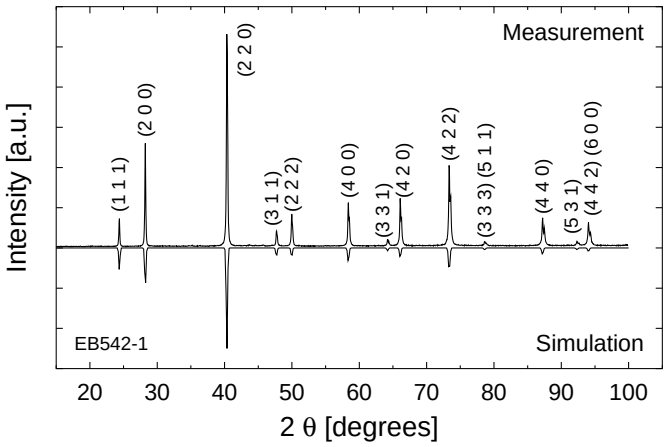

Figure 8.2: X-ray diffraction pattern of YNiSb in comparison to a simulated pattern. Lattice constant: 6.318 Å.

8.2.2 Solid-state reaction

Powdered elements (or — again — premelted binaries) were pressed to pellets in their stochiometric mixture. After sealing them in an evacuated quartz ampoule, the pellets were heated up slowly to about 800 – 900 °C to react the materials. The samples were then annealed at this temperature for several days. The pellet was powdered and annealed again two times.

Although the stochiometry can be controlled better with this technique, contamination with different impurities cannot be prevented in several powdering steps. According to the x-ray patterns, this technique also leads to one-phase material. However, sometimes traces of unidentified impurities are observed.

8.3 Electronic and Lattice Properties

Several samples in the YNiSb group have been prepared and investigated for their thermoelectric properties. The work focuses on the electronic properties to determine the power factor $S^2\sigma$. To estimate the figure of merit ZT thermal conductivity measurements have been carried out on one sample.

8.3.1 Properties of the Pure Compounds

Electrical Conductivity

All samples showed an activated behavior in the electrical conductivity. As an example, two resistivity curves are plotted in figure 8.3 for different samples of YNiSb.

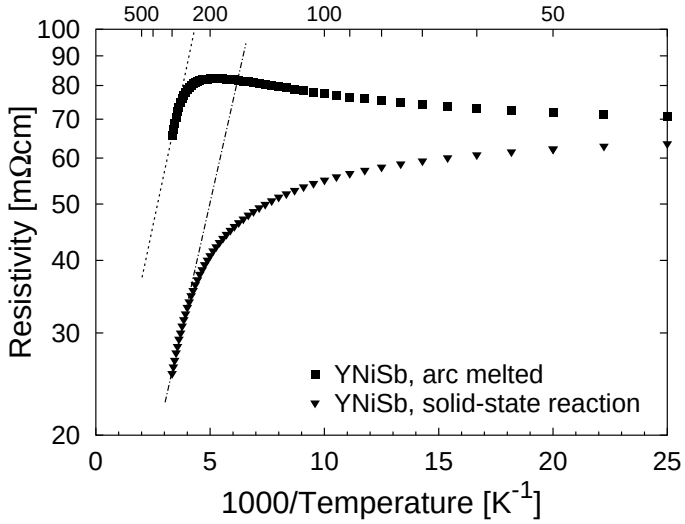

Figure 8.3: Resistivity of two differently prepared YNiSb samples. Both samples show an activated behavior with an activation energy of about 70 meV.

[Larson99] predicts a band gap of 280 meV for YNiSb in his band structure calculations, whereas in [Sportouch99], a band gap of about 90 meV is reported from infra-red spectroscopy. The activation energies calculated for the two samples (74 meV and 69 meV, respectively) agree fairly well with the latter value.

Seebeck Effect

All undoped samples prepared in this work exhibit *p*-type behavior. Among the investigated samples, YPtSb and ScNiSb exhibit thermopowers above 200 μV/K. But due to their higher resistivities, the power factor stays about one order of magnitude behind the state of the art material Bi_2Te_3.

Sample		activation energy [meV]	resistivity [mΩcm]	Seebeck coeff. [μV/K]	power fact. [10^{-3} W/K^{2}m]
EB560	YNiSb	73.6	65.5	80	0.010
JT001	YNiSb	69.3	25.5	115	0.052
EB550	YPtSb	2.7	20.5	230	0.258
EB554	ScNiSb	65.2	42.5	222	0.116
EB552	LuAuSn	metallic	0.15	4.5	0.014
EB553	ScAuSn	143.5	1.9	48	0.121
EB571	ErAuSn	29.9	0.3		

Table 8.1: Comparison of some YNiSb related compounds. The activation energy is based on the resistivity measurements. Resistivity, Seebeck coefficient, and power factor are measured at room temperature (300 K).

However, all these materials have not been optimized. And the third key quantity for the figure of merit ZT, the thermal conductivity κ of most compounds could not be measured in this work. Because of the complex crystal structure, it is expected to be very low. For the undoped ternary compounds, [Sportouch99] revealed thermal conductivities in the range of $4-6$ W/Km.

By alloying of two or more iso-electronic compounds, this value might drop significantly. Together with proper doping, this might lead to a competitive thermoelectric material. Therefore, several samples were prepared to investigate the effects of doping and alloying.

8.3.2 Doping in the YNiSb Group

The intention of this work was to screen the YNiSb group to identify interesting compounds for further investigations. Some studies with doped samples of the group have therefore been carried out. The goal is to explore whether the power factor can be increased by appropriate doping.

Doping can be achieved by two approaches: by non-stochiometry or by partially substituting some atoms in the crystal lattice. For the latter the valence electron number usually determines whether the dopant acts as a donator or an aceptor. The effect of the former method cannot generally be predicted.

For the solid-state reacted samples, the non-stochiometry method was used. YNiSb was prepared with 3% antimony excess, with the result shown in figure 8.4. As expected, the resistivity drops due to the increased carrier density. The excessive antimony acts as a p-type dopant.

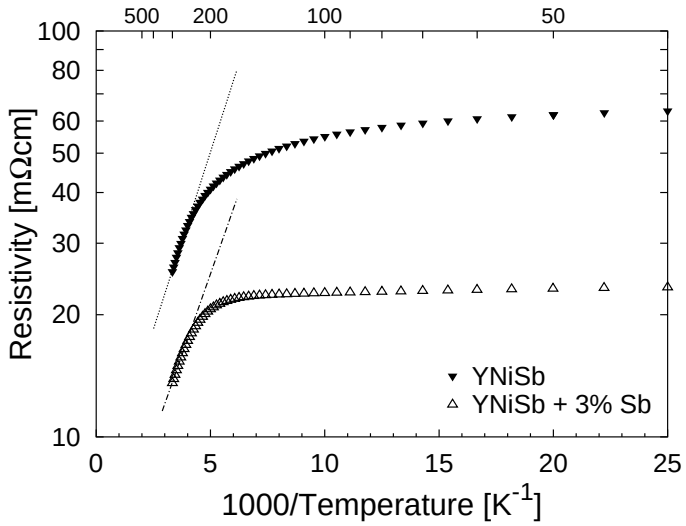

Figure 8.4: Doping effect on the electrical resistivity of YNiSb. To one of the two solid-state reacted samples 3% antimony were added. As expected, the resistivity drops, due to the increased carrier density, while the activation energy is unchanged.

At the same time the increase in the carrier density is reflected in the thermopower. As listed in the overview in table 8.2, the Seebeck power significantly dropped together

with the electrical resistivity. The activation energy of the doped compound stayed constant.

Sample		resistivity [mΩcm]	Seebeck coeff. [μV/K]	power fact. [10^{-3} W/K^{2}m]
JT001	YNiSb	25.5	115	0.052
JT003	$YNiSb_{1.03}$	13.6	69	0.035
JT010	$YPdSb_{0.5}Bi_{0.5}$	9.1	152	0.254
EB572	$(YNiSb)_{0.98}(MgCoSn)_{0.02}$	1.36	97	0.692
EB573	$Y_{0.98}Zr_{0.02}NiSb_{0.98}Te_{0.02}$	2.08	-54	0.214
EB570	$ZrYNi_2SnSb$	0.22	-12	0.065
EB574	ZrNiSn + ZrPtBi + ErPdSb, *n*-doped	1.8	-54	0.162

Table 8.2: Overview of some doped and alloyed compounds in the YNiSb group. Except for JT003, all the doped materials exhibited metallic behavior in their resistivity.

Doping is also the way to produce *p*- and *n*-type thermoelectrics. For a thermoelectric device both types are needed, but not all materials show good performance for both types. *p*-type Tl_9BiTe_6, as an instance, appears to exhibit much higher performance than its *n*-type counterpart (see chapter 7). Larson *et al.* predict higher thermopowers at room temperature for *n*-type YNiSb [Larson99, sec. E.], based on their calculations of the effective hole masses.

Two samples of YNiSb are shown in figures 8.5(a) and 8.5(b) with *p*-type and *n*-doping. These measurements prove that YNiSb can indeed be doped *n*-type. However, in contrast to the theoretical prediction the *n*-type sample exhibits a higher resistivity *and* a lower thermopower than the *p*-type material.

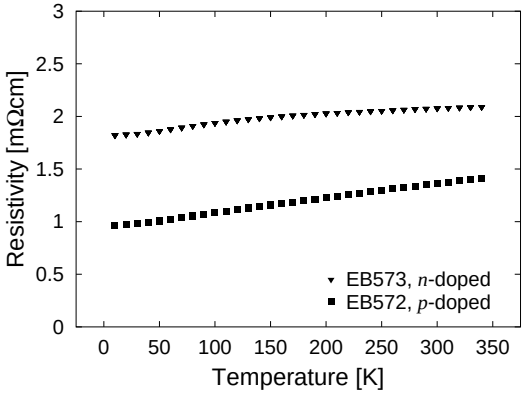

(a) Resistivity of a *p*- and a *n*-doped YNiSb compound

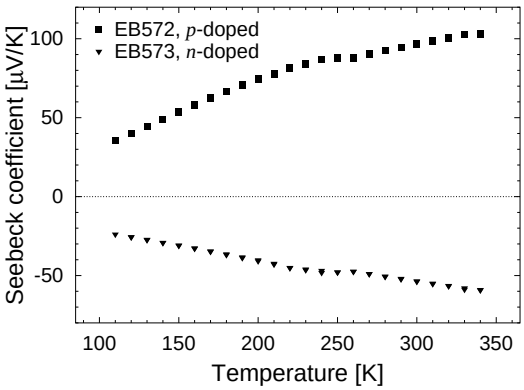

(b) Seebeck coefficient of a *p*- and a *n*-doped YNiSb compound

Figure 8.5: Electrical resistivities and Seebeck coefficients of a *p*- and a *n*-doped compound in the YNiSb group.

8.3.3 Alloying in the YNiSb Group

Alloying has been a very important step in the improvement of several thermoelectric materials. While lowering the lattice thermal conductivity by introducing mass fluctuations, this technique can be expected to have only little influence on the electronic properties of the material. In the YNiSb group alloying is not only possible on one or two of the lattice sites, as in the related ZrNiSn group. All three elements can be replaced by an iso-electronic element. This promises many possibilities for lowering the thermal conductivity.

Thermal Conductivity — Measurement Setup

For the measurements on the YNiSb related compounds and the $Zr_3Ni_3Sb_4$ related compounds (see next chapter) a steady-state method was used. To reduce the heat loss in this widely used technique, a modified method was developed.

The steady state method is a straight-forward translation of the 4 point probe technique used for the electrical resistivity. One end of a sample rod with known geometry is mounted on a heat sink. With a resistive heater on the other end of the rod, a known heat flow ($P = R \cdot I^2$) is introduced in the sample. A thermocouple measures the temperature gradient along the sample and the conductivity is calculated as $Pd/A\Delta T$. In our measurements a temperature gradient of 1 Kelvin along the thermocouple distance of about 5 mm was applied.

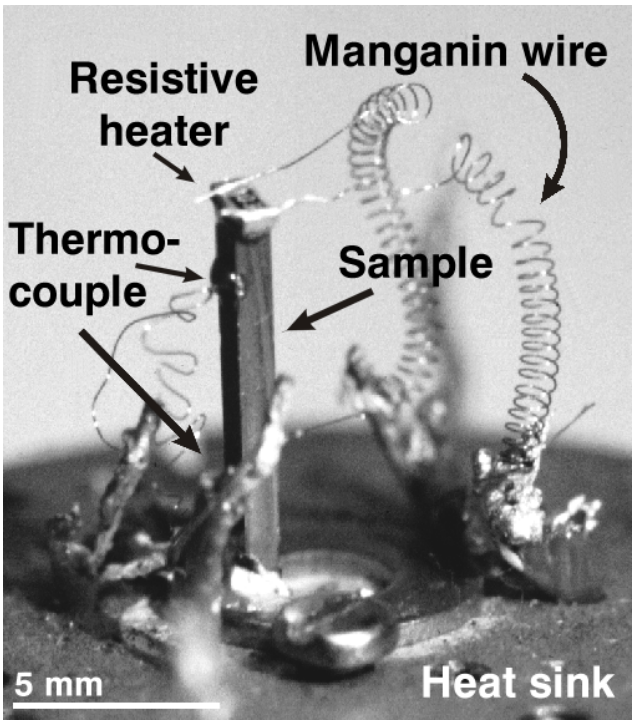

Figure 8.6: Picture of a thermal conductivity sample using the steady-state method. The heat shield as described in the text would be put over the whole setup.

This result, however, is only valid under the assumption of that heat is solely conducted through the sample. However, if the conductivity of the sample is very low, different loss mechanisms have an important impact on the heat flow.

Most of these losses can be minimized by a well-designed sample setup. The contact wires for heater and thermocouple are held as long as possible and rolled up in a spiral shape to reduce the heat flow along these wires. A manganin wire was chosen for the contact wires of the heater. Its thermal conductivity is about one order of magnitude lower than the conductivity of other commonly used metals [Weast84, sec. E-9]. The use of a long and thin wire reduces the electrical conductivity of the wire which lowers the electronic part of the thermal conductivity (see Wiedemann-Franz law, section 2.3.4).

To minimize energy losses in the wires, a high resistance of 10 kΩ was chosen for the heater. Convection losses are eleminated by carrying out the measurements under a vacuum of approximately 10^{-4} Torr.

However, with increasing temperature another contribution becomes important. Radiative losses have an important impact for temperatures above ∼150 Kelvin.

These losses can be minimized by the use of a controlled heat shield. A metal shield as shown in figure 8.7 is covering the whole setup. This shield is in good thermal contact with the heat sink and has another resistive heater on top. This heater is controlled in a way that the temperature gradient along the sample and on the heat shield are equal. Radiative heat between sample and heat shield should now be in an equilibrium with a net heat flow of zero.

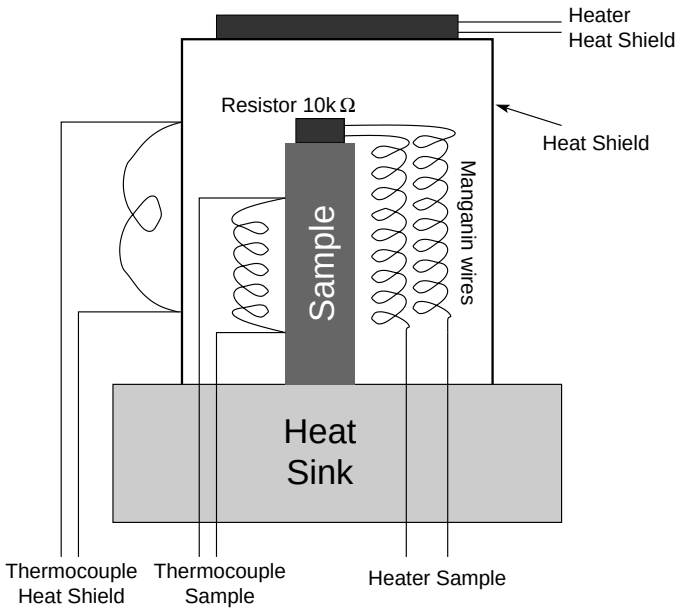

Figure 8.7: Setup for the steady-state method to measure thermal conductivity.

Both heaters now influence each other, which makes the system hard to control manually. A computer-controlled system has therefore been set up to control the measurement process.

The accuracy of the setup after these improvements is mainly determined by uncertainties in the sample geometry and in the distance of the thermocouples on the sample. The requirements for this technique are therefore a sufficiently large and homogeneous sample (at least 1×1×10 mm) with a well defined shape.

Reference measurements on Pyrex glass showed a very effective elimination of the radiation losses and a high accuracy of this method.

Thermal Conductivity — Results

For the ternary YNiSb related compounds, thermal conductivities in the range of 4–6 W/Km (6.1 W/Km for YNiSb) are reported [Sportouch99]. In figure 8.8, half of the Sb atoms of YPdSb have been replaced by Bi. This results in a thermal conductivity for $YPdSb_{0.5}Bi_{0.5}$, that is significantly lower than all values reported by [Sportouch99]. For room temperature a thermal conductivity of 2.9 W/Km was revealed.

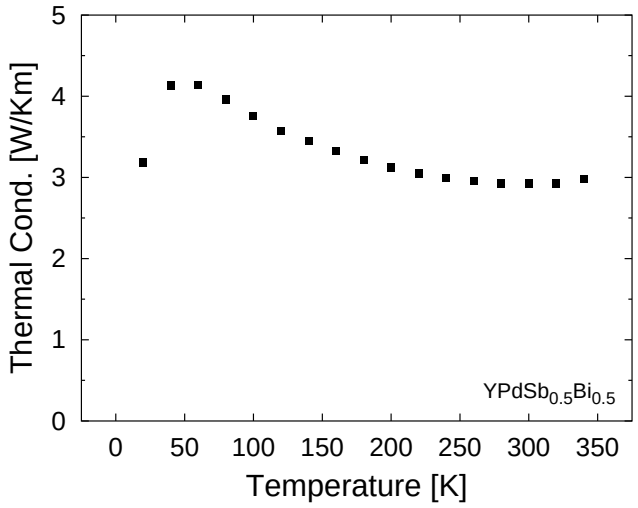

Figure 8.8: Thermal conductivity of the $YPdSb_{0.5}Bi_{0.5}$ alloy. The conductivity is significantly lower than the values that [Sportouch99] reports for the ternary compounds.

Several alloys with replacements on the other lattice sites have been prepared and proven to exist. Due to the lack of sufficiently large samples of high quality, no further measurements were possible.

The existence of those phases, in conjunction with the success on the Sb site, however, suggests that further reduction of the thermal conductivity is possible by alloying on the other lattice sites. This is also supported by successful reports of alloying in closely related systems, e. g. the ZrNiSn system, where the thermal conductivity was halved in $Zr_{0.5}Hf_{0.5}NiSn$ [Hohl97].

Electronic Properties

A reduction of the thermal conductivity by alloying only makes sense if the power factor is not significantly reduced. The properties of sample EB574 (see table 8.2), which is a

doped alloy between three materials with the Half-Heusler structure (ZrNiSn, YPtBi, and ErPdSb), show that even complex alloys exhibit reasonably high thermopowers.

Unfortunately, no sufficiently large sample could be prepared for accurate measurements of the thermal conductivity. But with the results from the previous section in mind, the thermal conductivity is expected to be lower than in the ternary compounds.

8.4 Conclusions

A number of YNiSb related compounds has been screened for their thermoelectric performance. Some of them show reasonably high thermopowers and electrical conductivities. Doping and impurities appear to have a strong influence on these quantities.

The thermal conductivity could only be measured on one sample. By alloying on one crystal site, a very low thermal conductivity was measured, in comparison to published results on similar materials. The general effect of alloying on the thermal conductivity is still a matter of discussions. Several suggestions have been published, but they are often limited to very specific systems. The YNiSb group is an interesting material from this research point of view. In further studies the alloying effect could be investigated on all three lattice sites.

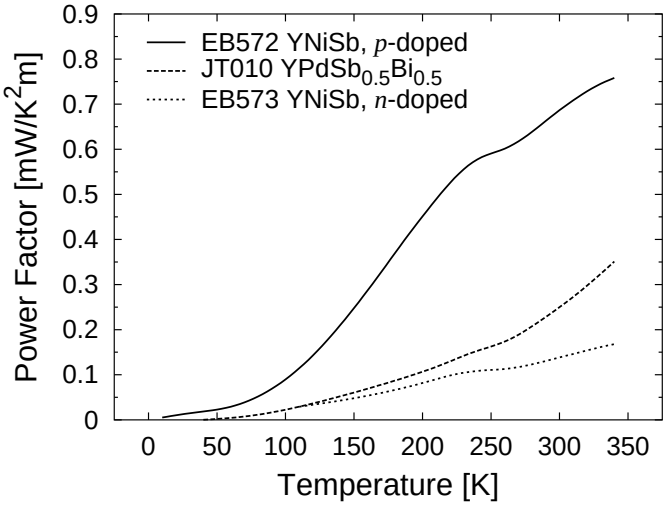

Figure 8.9: Power factors of the best materials investigated in this group. For the doped YNiSb compounds no thermal conductivity data are available to calculate ZT. For JT010 ZT, equals 0.04 at room temperature.

Figure 8.9 shows the power factor of three samples. Currently, these compounds cannot compete with other materials. With optimized samples, a higher ZT for elevated temperatures seems possible.

9 The $Zr_3Ni_3Sb_4$ Group

A structure closely related to the Half-Heusler structure is the $Y_3Au_3Sb_4$ type structure. By expanding the formula unit of the MgAgAs type structure to $Mg_4Ag_4As_4$ and reducing the atom number of two elements by one, the more complex $Y_3Au_3Sb_4$ type structure is formed. Compared to the MgAgAs structure, a lower thermal conductivity is therefore expected for this structure.

As already mentioned in the previous chapter, some Half-Heusler phases reported in the literature showed a fairly good thermoelectric performance. The crucial problem with these materials, however, has always been the thermal conductivity. The $Zr_3Ni_3Sb_4$ related compounds might combine good electronic performance with an expected low thermal conductivity.

9.1 Known Compounds and Properties

The ternary pnictides $M_3M'_3Pn_4$ form a large group of materials. They have been studied for their many different electronic effects. Within this group, Kondo insulators, superconductors and magnetoresistive materials have been found. Some of the materials have also attracted attention for the use as thermoelectric materials.

The thermoelectric properties have been studied on $R_3Cu_3Sb_4$ (R = La, Ce, Gd, Er) [Fess97, Fess98] and the Kondo insulator $Nd_xCe_{3-x}Pt_3Sb_4$ [Jones98, Jones99] These materials only showed moderate thermoelectric performance with $ZT = 0.1$ at 400 K and $ZT = 0.12$ at 230 K, respectively. Both groups, however, report a thermal conductivity in the range of 2 – 4 W/Km. As expected, this value is reasonably low and makes the group interesting for thermoelectric applications.

Wang *et al.* showed the existence of $Zr_3Ni_3Sb_4$, $Hf_3Ni_3Sb_4$ and $Zr_3Pt_3Sb_4$ and characterized their lattice structure [Wang99]. They also published band structure calculations which predicted a small band gap of 0.5 meV. This indicates interesting thermoelectric performance.

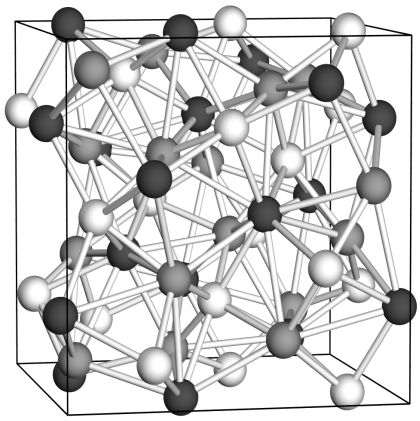

Figure 9.1: The $Zr_3Ni_3Sb_4$ structure. Zirconium atoms are black, antimony dark grey. The very complex cubic structure is based on a modification of the MgAgAs structure.

9.2 Sample Preparation and Crystal Structure

$Zr_3Ni_3Sb_4$ and two modifications have been prepared by the arc melting method described in chapter 8. To investigate the effects of doping on these materials, *p*- and *n*-doped samples were prepared in addition to the pure compounds.

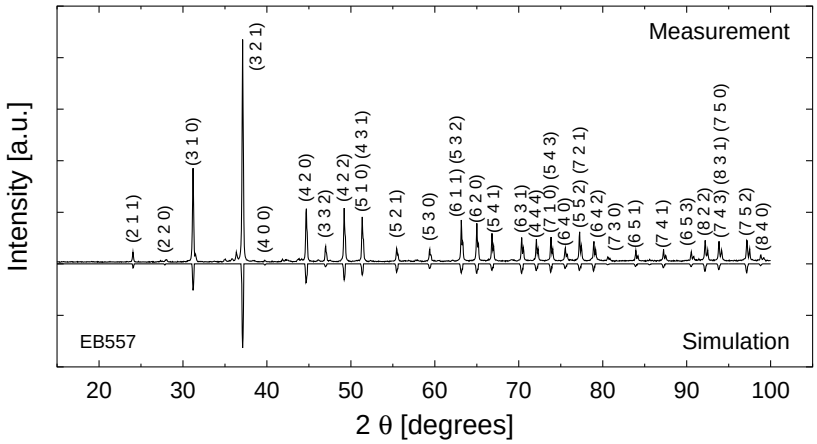

Figure 9.2: X-ray diffraction pattern of $Zr_3Ni_3Sb_4$ in comparison to a calculated pattern. Lattice constant: 9.075 Å.

X-ray diffraction patterns showed that all samples were phase pure and had the $Y_3Au_3Sb_4$ structure (space group $I\bar{4}3d$, Pearson symbol $cI40$). The pattern of $Zr_3Ni_3Sb_4$ is given in figure 9.2 as an example. A ball-and-stick representation of $Zr_3Ni_3Sb_4$ is shown in figure 9.1. The cubic unit cell is formed by 40 atoms.

9.3 Electronic Properties

All pure and *p*-doped samples show an activated behavior, which is in good agreement with the Grimm-Sommerfeld rule and the band structure calculations. The activation

energy, deducted from the decrease of the resistivity with temperature, varies between 150 and 220 meV for the undoped compounds. Doping significantly decreases this activation energy to the range of 27 to 100 meV.

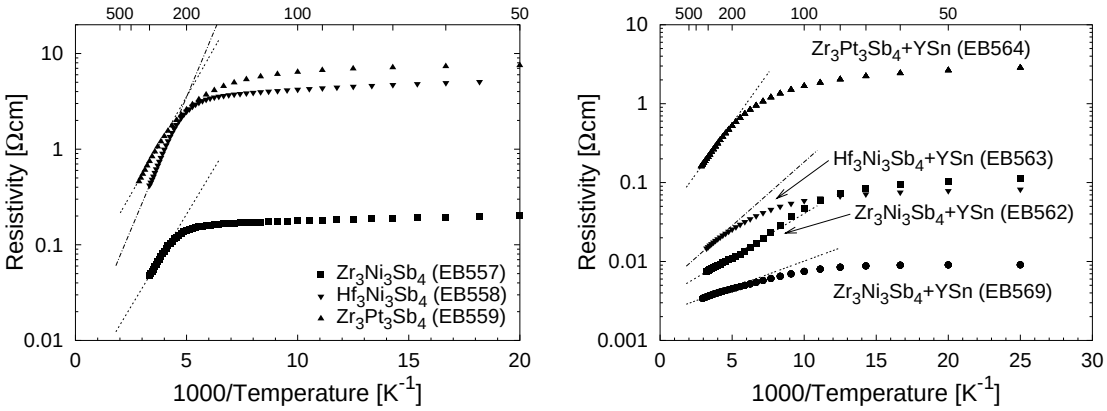

(a) Resistivity of undoped samples

(b) Resistivity of doped samples

Figure 9.3: Electrical resistivities of doped and undoped $Zr_3Ni_3Sb_4$ group members.

In figures 9.3(a) and 9.3(b) the resistivity of the undoped and doped compounds are compared. While moderate doping strongly impacts the electrical conductivity, the Seebeck coefficient is decreased only sparsely. The thermopower shows typical behavior and its maximum is not reached in the investigated temperature range up to 340 K. All the data are summarized in table 9.1.

Sample	activation energ. [meV]	resistivity [mΩcm]	Seebeck [μV/K]	power fact. [10^{-3} W/K^{2}m]
EB557 $Zr_3Ni_3Sb_4$	153	48	238	0.118
EB558 $Hf_3Ni_3Sb_4$	220	420	205	0.010
EB559 $Zr_3Pt_3Sb_4$	162	747	390	0.020
EB562 $Zr_3Ni_3Sb_4 + 1\%$ Y, Sn	43	8	220	0.633
EB569 $Zr_3Ni_3Sb_4 + 2\%$ Y, Sn	27	4	99	0.270
EB563 $Hf_3Ni_3Sb_4 + 1\%$ Y, Sn	44	15	208	0.283
EB564 $Zr_3Pt_3Sb_4 + 1\%$ Y, Sn	101	211	290	0.040
EB568 $Zr_3Ni_3Sb_4 + 2\%$ Nb, Te	met.	0.37	–59	0.941

Table 9.1: Comparison of some $Zr_3Ni_3Sb_4$ related compounds. The activation energy is based on the resistivity measurements. Resistivity, Seebeck, and power factor are measured at room temperature (300 K). Sample EB568 shows metallic behavior.

With sample EB568, one test was made to *n*-dope $Zr_3Ni_3Sb_4$. At the rather high doping level of 2 % Te and Y, the material became metallic. The electrical conductivity became very high in this experiment (2700 Ω^{-1}cm^{-1}), resulting in a power factor of 0.94 mW/K^{2}m. With –59 μV/K the thermopower of this sample, however, is too low for a competitive thermoelectric material (see section 2.4.2).

In all cases, doping had a strong impact on the thermoelectric performance. For the $Zr_3Ni_3Sb_4$ compound, the power factor was increased by a factor of six, up to $0.6\,\mathrm{mW/K^2m}$.

9.4 Thermal Conductivity

The thermal conductivity is expected to be very low in these materials. As mentioned above, values below 4 W/Km were reported for other compounds with the $Y_3Au_3Sb_4$ structure. To give an estimation for the thermal conductivity of the $Zr_3Ni_3Sb_4$ related compounds, sample number EB562 was chosen to be measured. It shows a good power factor and has a high Seebeck coefficient.

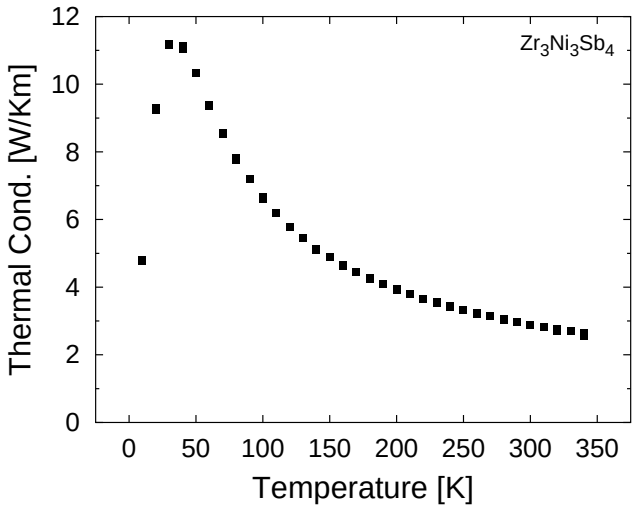

Figure 9.4: Thermal conductivity of p-doped $Zr_3Ni_3Sb_4$. It is strongly dominated by the lattice contribution. The electronic part contributes less than 5 % over the whole temperature range.

The result, shown in figure 9.4, confirms the published values. At room temperature a value of 2.9 W/Km was measured. The thermal conductivity is strongly dominated by the lattice conductivity. In the high temperature region, the curve follows a T^{-x} law, where x is calculated to 0.75 by a fit to the measurement data. In a simplified theory for ideal crystals, a T^{-1} law is predicted for phonon-phonon scattering in the high temperature region. Because of an increasing phonon number at higher temperatures, the free phonon path decreases as T^{-1}. With an almost constant C_V, the thermal conductivity follows the T^{-1} law, too (see formula 2.40 on page 13).

In a non-perfect material, however, exponents can be expected between $x = 0$ and $x = 3$ — depending on the contribution of different phonon scattering mechanisms [Berman79, sec. 8.2.1]. Defect scattering should make a temperature independent contribution.

The influence of complex crystal structures or alloys can be treated as defect scattering. $Zr_3Ni_3Sb_4$ has a very complex crystal structure, which is reflected in the thermal

conductivity by a T^{-x} law with $x < 1$. The structure therefore has indeed a strong influence on the low thermal conductivity.

The expectations that the $Zr_3Ni_3Sb_4$ type materials has a lower thermal conductivity than the Half-Heusler structured compounds is confirmed by these measurements. The origin is the more complex unit cell that increases phonon-scattering.

9.5 Conclusions

The performance of the $Zr_3Ni_3Sb_4$ related compounds is comparable to the YNiSb group. The power factors are strongly dependent on the stochiometry and on doping. But they are too low to compete with state of the art materials. The base compounds are all p-type, but with doping the n-type counterpart can be prepared. For one p-doped sample, thermal conductivity measurements have been carried out and the dimensionless figure of merit was determined to 0.07 at 300 K. Higher efficiencies are expected at elevated temperatures. Related materials are reported to reach their maximum figure of merit at 700 K or higher [Hohl99].

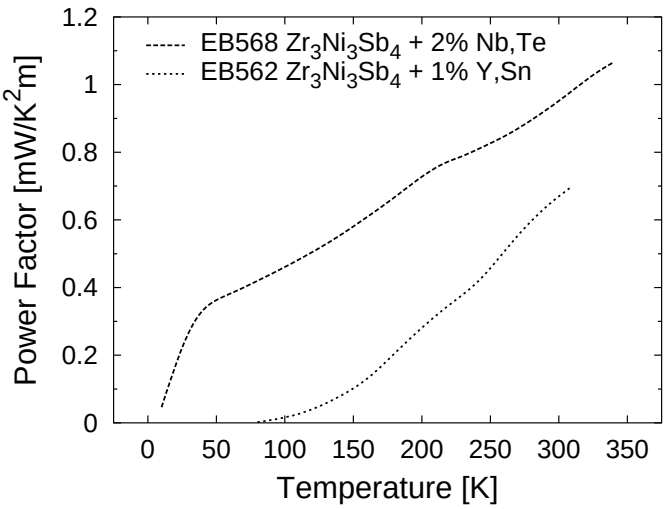

Figure 9.5: Power factor of the two $Zr_3Ni_3Sb_4$ related samples that show the best performance in this work. The p-doped sample (EB562), has a dimensionless figure of merit of 0.07 at room temperature.

The more complex structure compared to the YNiSb related compounds leads to a lower thermal conductivity. But in contrast to YNiSb the number of iso-electronic compounds is lower. Therefore the possibilies to limit the thermal conductivity or fine-tune the electronic properties by alloying are more limited.

The materials in the $Zr_3Ni_3Sb_4$ group show reasonable thermoelectric performance, in particular $Zr_3Ni_3Sb_4$, which exhibits a high thermopower and a low thermal conductivity. The high electrical resistivity, however, limits the thermoelectric performance. The $Zr_3Ni_3Sb_4$ group itself will therefore not replace the current state of the art materials, but further research in related systems is still promising.

10
Conclusions and Outlook

The objective of this work has been to investigate the possibilities to optimize thermoelectric materials. Three main approaches have been studied:

- The alloy system $Tl_9Sb_{1-x}Bi_xTe_6$ has been characterized in order to tune the electronic properties and reduce the thermal conductivity of Tl_5Te_3 compounds.
- Doping studies have been carried out to improve the power factor of Tl_9BiTe_6.
- The thermoelectric performance of two new promising groups was investigated: the YNiSb- and the $Zr_3Ni_3Sb_4$-related compounds.

Studies on the Alloy System Tl_9SbTe_6–Tl_9BiTe_6

As a basis for studies on the alloy system Tl_9SbTe_6–Tl_9BiTe_6, the ternary compound Tl_9SbTe_6 has been synthesized. For a thorough investigation, high purity material was produced by zone refining.

Detailed transport measurements on Tl_9SbTe_6 are reported in this work for the first time. The electrical conductivity was found to be very high and exceeds the conductivity of Tl_9BiTe_6 by a factor of six. At the same time, however, the Seebeck coefficient is reduced from 281 μV/K for Tl_9BiTe_6 to 101 μV/K for Tl_9SbTe_6. This results in a slightly lower power factor of 0.66 mW/K^{2}m as compared to Tl_9BiTe_6 (0.9 mW/K^{2}m).

A slightly higher thermal conductivity was measured in Tl_9SbTe_6, compared to the values reported for Tl_9BiTe_6 (0.76 W/Km vs. 0.49 W/Km). This can be explained by a larger electronic contribution, while the lattice conductivity is changed only slightly. As opposed to the T^{-1} law in Tl_9BiTe_6, the lattice contribution in Tl_9SbTe_6 stays almost constant over a large temperature range, close to Slack's lower limit for this compound ($\sim$ 0.2 W/Km), which indicates a much stronger disorder-scattering in Tl_9SbTe_6 than in Tl_9BiTe_6.

The thermoelectric figure of merit ZT was determined to be 0.26 at room temperature. In the investigated temperature range up to 340 K, ZT increases monotonically.

There is no visible indication of a maximum, but as the compound is closely related to Tl_9BiTe_6, it is expected in the range of 400 to 450 K. Thus, Tl_9SbTe_6 was found to be a very good thermoelectric material, but with its lower thermopower it stays behind Tl_9BiTe_6, which still has to be considered as the best ternary compound in the Tl_5Te_3 group. The figure of merit of both compounds is depicted in figure 10.2, where they are compared to a *p*-doped Tl_9BiTe_6 sample.

In order to study the alloy system $Tl_9Sb_{1-x}Bi_xTe_6$, alloys of different compositions have been prepared and characterized. Theoretical estimations on the electronic properties have been made that suggest a maximum power factor for alloys with $x \approx 0.7$. This has been confirmed by actual measurements and the power factor was improved by about 10 %.

This increase in the power factor, however, was found to be compensated by a higher thermal conductivity. Alloying does not lead to the expected lowering of the lattice contribution. Instead, the trend of the thermal conductivity is dominated by the electronic contribution and thus increases almost linearly from Tl_9BiTe_6 to Tl_9SbTe_6. Therefore, alloying does not lead to an improved thermoelectric figure of merit *ZT* and Tl_9BiTe_6 still exhibits the best thermoelectric performance in this alloy system, as depicted in figure 10.1.

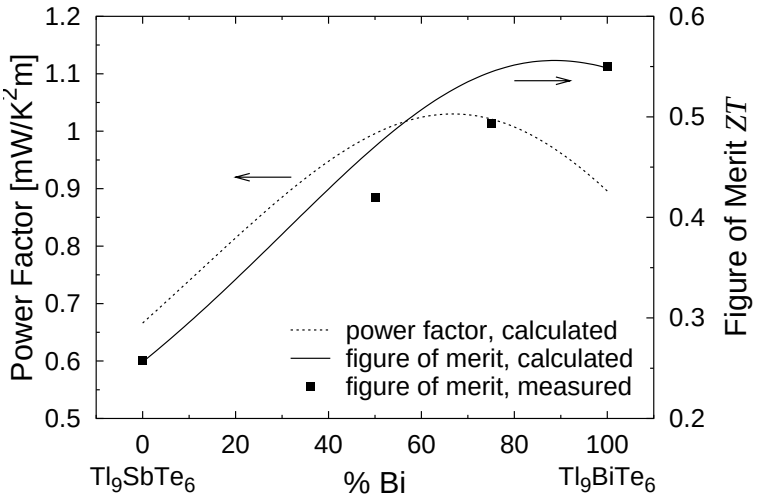

Figure 10.1: Thermoelectric performance of the Tl_9SbTe_6–Tl_9BiTe_6 alloy system. The power factor (dotted line) was calculated based on the electronic properties of the end compounds. Combining it with a linear interpolation of the measured thermal conductivities results in the figure of merit that is shown as a solid line. The squares are the actually measured *ZT*.

Doping Effects in Tl_9BiTe_6

The second approach to optimize Tl_9BiTe_6 was to tune the electronic properties by doping. This includes the formation of *n*-type material, as for a thermoelectric device both types of materials are needed.

Extensive studies have been carried out that prove the possibility to produce *n*-type Tl_9BiTe_6 by doping with bismuth. At lower doping levels, however, the material becomes semiconducting with a high resistivity. With stronger doping, the Seebeck coefficient drops significantly. Therefore, *n*-doped Tl_9BiTe_6 does not seem to be a competitive thermoelectric material.

The effect of *p*-doping was studied by using HgTe as a dopant. An increase in the electrical conductivity was observed due to a higher charge carrier density. Nevertheless, for moderate doping levels the Seebeck coefficient stays almost unaffected. The highest power factor so far has been observed in $Tl_9BiTe_6 + (HgTe)_{0.16}$. At 300 K the power factor was increased by approximately 20 %, compared to zone refined Tl_9BiTe_6. In combination with the known extremely low thermal conductivity, this results in a dimensionless figure of merit of $ZT = 0.75$ at room temperature (compared to 0.63 for Tl_9BiTe_6). The temperature dependence of $Tl_9BiTe_6 + (HgTe)_{0.16}$ is shown in figure 10.2 in comparison to purified Tl_9BiTe_6 and Tl_9SbTe_6.

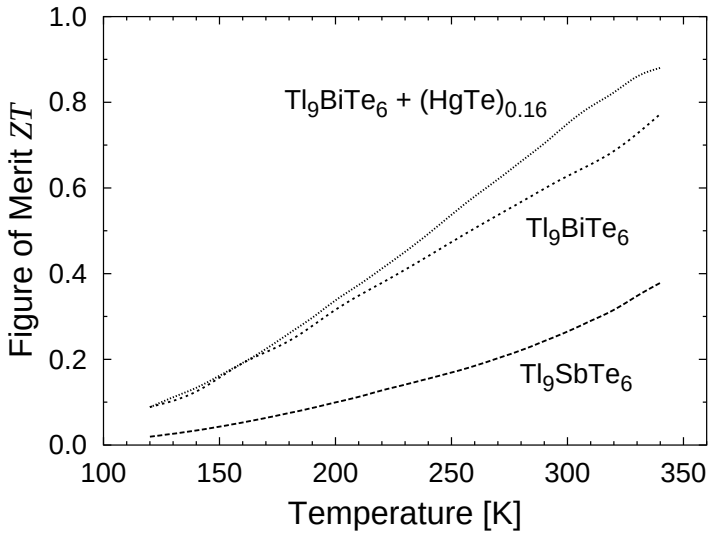

Figure 10.2: Comparison of the thermoelectric figure of merit ZT for the purified ternary compounds Tl_9BiTe_6 and Tl_9SbTe_6, and a *p*-doped Tl_9BiTe_6 sample.

The improvement of the thermoelectric properties, however, goes along with an increased brittleness of the material. This already caused difficulties in sample preparation and handling and is very likely to make the material unsuitable for real devices. Nevertheless, it has been shown that the thermoelectric properties of Tl_9BiTe_6 can be improved significantly by proper doping. This is promising for further investigations focusing on different dopants and/or doping techniques, which may circumvent the problems of mechanical stability and lead to further enhancement of the power factor of Tl_9BiTe_6.

The New Groups YNiSb and $Zr_3Ni_3Sb_4$

In additional studies, the thermoelectric performance of two new groups of materials has been investigated. The YNiSb related compounds crystallize in the Half-Heusler structure. Similar materials with this structure show good thermoelectric performance, as first reported by [Hohl97]. The compounds of the $Zr_3Ni_3Sb_4$ group crystallize in the related $Y_3Au_3Sb_4$ structure.

All undoped samples show semiconducting behavior. For the YNiSb related compounds, resistivities between 20 and 65 mΩcm were measured, with Seebeck coefficients up to 230 μV/K. Significant improvement of the power factors was achieved by doping. However, in all cases the power factor and/or the thermopower are too low to make these materials really promising.

All undoped samples show *p*-type behavior. With doping, also *n*-type material has been synthesized. As opposed to theoretical predictions, the *n*-type compounds exhibit a lower thermopower *and* a lower electrical conductivity than *p*-type material and have therefore lower power factors.

In the $Zr_3Ni_3Sb_4$ group stronger variations of the thermoelectric properties are found. Except for a highly doped sample, all prepared samples in this group show semiconducting behavior with resistivities between 4 and 750 mΩcm. The low resistivity samples, however, have too low thermopowers ($\sim$200 μV/K) to be competitive with state of the art materials. The power factor was improved by doping.

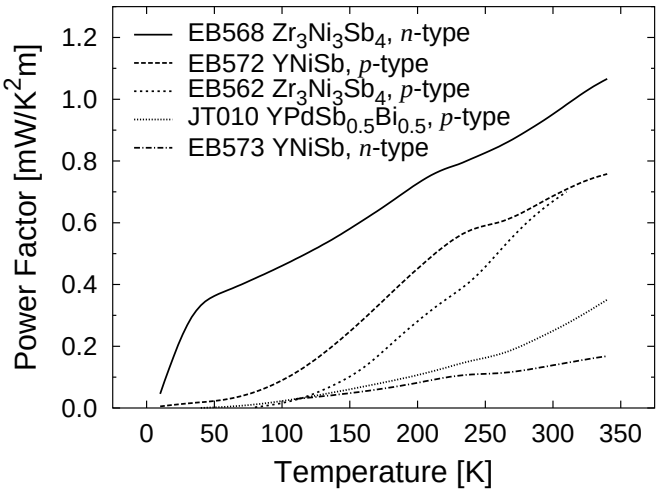

Figure 10.3: Power factor of some materials in the YNiSb and $Zr_3Ni_3Sb_4$ group. For samples EB562 and JT010 the thermal conductivity was determined to 0.2 W/Km, which results in a figure of merit ZT of 0.07 and 0.04, respectively. The other samples are expected to exhibit similar thermal conductivities.

The crystal structure of both material groups (YNiSb and $Zr_3Ni_3Sb_4$) suggests a low thermal conductivity. The thermal conductivity of the latter group was determined to 2.9 W/Km. In the former group the same value was measured on a sample with a 50 % substitution on the Bi lattice site, while higher values were reported in the literature for

the pure ternary compounds [Sportouch99]. The complex crystal structure therefore indeed exhibits a low thermal conductivity. Alloying leads to a further reduction. Substitutions on the two other lattice sites are expected to reduce the thermal even more.

In figure 10.3 the power factor of some representatives of both groups is shown. For two of the samples the thermal conductivity was measured, which resulted in a figure of merit of 0.07 for *p*-type $Zr_3Ni_3Sb_4$ (EB562) and 0.04 for *p*-type $YNiSb_{0.5}Bi_{0.5}$ (JT010), respectively. In all materials a higher figure of merit is expected for elevated temperatures. The power factor shows no indications of a maximum up to 340 K, and all materials have very high melting points, which would allow the use at high temperatures. In related materials, the maximum power factor was observed above 700 K [Hohl99].

Although the materials have not been fully optimized, the two classes of the YNiSb related and the $Zr_3Ni_3Sb_4$ related compounds show high thermopowers with low thermal conductivities. The electrical resistivity, however, is too high for a competitive thermoelectric material. Nevertheless, research in related groups might lead to materials with a competitive performance.

Outlook

Three different classes of materials for thermoelectric applications have been investigated in this work and various approaches have been made to optimize these materials. Although the research in the YNiSb and $Zr_3Ni_3Sb_4$ group has led to interesting results, it seems that a really competitive thermoelectric material has yet to be found in these groups.

In the Tl_5Te_3 group, significant progress has been made by improving the thermoelectric properties of Tl_9BiTe_6 by doping with HgTe. A dimensionless figure of merit of $ZT = 0.75$ has been achieved at room temperature, which represents an enhancement of approximately 20 % over undoped material. Even though this improvement goes along with an increased brittleness of the material, which makes it probably unsuitable for applications, this result is very important for future investigations. It clearly shows, that further optimization of Tl_9BiTe_6 is possible and we can expect that different dopants lead to higher power factors without compromising the integrity of the material.

Symbols

α	thermal expansion coefficient
χ	compressibility
C_V	specific heat at constant volume
e	elementary charge
ε	reduced energy $\frac{E}{k_\mathrm{B}T}$
ε_F	reduced Fermi energy
E	electric field
E	energy
E_F	Fermi energy
f_0	Fermi-Dirac distribution function
$F_j(\varepsilon)$	Fermi integral
γ	Grüneisen parameter
h	Planck constant (6.626×10^{-34} Js)
$\hbar$	Planck constant divided by 2π
η	efficiency
$\mathbf{j}$	(electrical) current density
$\mathbf{k}$	wave vector
$\mathbf{K}$	reciprocal lattice vector
k_B	Stefan-Boltzmann constant
κ	thermal conductivity
κ_e	electronic part of κ
κ_l	lattice part of κ
κ_min	minimum lattice conductivity
l	mean free path
L	Lorenz number
m^*	effective mass
m_e	free electron mass
μ	electron/hole mobility
M	mean atomic mass
n	charge carrier density
N_0	Avogadro's number
Π	Peltier coefficient
r	scattering parameter
ϱ	electrical resistivity, mass density
R	universal gas constant
σ	electrical conductivity
S	Seebeck coefficient
t	time
τ	relaxation time, Thomson coefficient
τ_0	proportional factor for τ
T	absolute temperature
T_m	melting point
Θ_D	Debye temperature
$\mathbf{v}$	velocity
v_s	velocity of sound
V	voltage
$\mathbf{w}$	heat flow
ω	angular frequency
Z	thermoelectric figure of merit $\frac{S^2\sigma}{\kappa}$

Bibliography

[Abeles63] B. Abeles. *Lattice Thermal Conductivity of Disordered Semiconductor Alloys at High Temperature*. Physical Review, *131*, (1963) 1906–1911. 14

[Barchii88] I. E. Barchii, V. B. Lazarev, E. Y. Peresh, Y. V. Voroshilov and V. Tkachenko. *Phase Equilibria in $Tl_2Se(Te)$-$Bi_2Se_3(Te_3)$ and Tl_9Bi-$Se(Te)$ Systems and Properties of the Compounds Formed*. Izvestiya Akademii Nauk SSSR, Neorganicheskie Materialy, *24*, (1988) 1791–1795. 22

[Bardeen50] J. Bardeen and W. Shockley. *Deformation Potentials and Mobilities in Non-Polar Crystals*. Physical Review, *80*, (1950) 72. 12

[Berman79] R. Berman. *Thermal Conduction in Solids*. Oxford Studies in Physics. Oxford University Press, Oxford, 1979. 29, 64

[Bhan70] S. Bhan and K. Schubert. *Kristallstruktur von Tl_5Te_3 und Tl_2Te_3*. Journal of the Less-Common Metals, *20*, (1970) 229–235. 21

[Bucher99] E. Bucher. *Wahlpflichtvorlesung Halbleiterphysik*. Universität Konstanz (1999). 52

[Cahill90] D. G. Cahill. *Thermal Conductivity Measurement from 30 to 750 K: The 3ω Method*. Review of Scientific Instruments, *61*, (1990) 802–808. 19, 20

[Cahill92] D. G. Cahill, S. K. Watson and R. O. Pohl. *Lower Limit to the Thermal Conductivity of Disordered Crystals*. Physical Review B, *46*, (1992) 6131–6140. 15

[Callaway60] J. Callaway and H. C. von Baeyer. *Effect of Point Imperfections on Lattice Thermal Conductivity*. Physical Review, *120*, (1960) 1149–1154. 38

[Erginsoy50] C. Erginsoy. *Neutral Impurity Scattering in Semiconductors*. Physical Review, *79*, (1950) 1013–1014. 12

[Fess97] K. Feß. *Neue thermoelektrische Materialien — Untersuchungen an Halbleitern und unkonventionellen Materialsystemen*. Ph.D. thesis, Universität Konstanz (1997). 61

[Fess98] K. Feß, W. Käfer, C. Thurner, K. Friemelt, C. Kloc and E. Bucher. *Magnetic and Thermoelectric Properties of $R_3Cu_3Sb_4$ (R = La, Ce, Gd, Er)*. Journal of Applied Physics, *83*, (1998) 2568–2573. 61

[Goldsmid99] J. H. Goldsmid and H. W. Sharp. *Estimation of the Thermal Band Gap of a Semiconductor from Seebeck Measurements*. Journal of Electronic Materials, *28*, (1999) 869–872. 43

[Goldsmid00] J. H. Goldsmid and H. W. Sharp. *Boundary Scattering of Phonons: A New Approach*. In *Proceedings of the Nineteenth International Conference on Thermoelectrics, ICT 2000, Cardiff, Wales*. 2000. To be published. 14

[Heikes61] R. R. Heikes and R. W. Ure, Jr. *Thermoelectricity: Science and Engineering*. Interscience Publishers, New York, London, 1961. 12

[Hohl99] H. Hohl, A. P. Ramirez, C. Goldmann, G. Ernst, B. Wölfing and E. Bucher. *Efficient Dopants for ZrNiSn-based Thermoelectric Materials*. Journal of Physics: Condensed Matter, pages 1697–1709. 65, 71

[Hohl97] H. Hohl, A. P. Ramirez, W. Käfer, K. Feß, C. Kloc and E. Bucher. *A New Class of Materials with Promising Thermoelectric Properties: MNiSn (M=Ti, Zr, Hf)*. In *Thermoelectric Materials — New Directions and Approaches* (edited by T. M. Tritt, M. G. Kanatzidis, J. Hylan B. Lyon and G. D. Mahan), volume 478 of *Symposium Proceedings*, pages 109–114. Materials Research Society, Pittsburgh, PA, 1997. 3, 51, 59, 70

[Houenou81] P. Houenou and R. Eholie. *Etude du Diagramme Ternaire Tl-Sn-Se: Description du Quadrilatère $SnSe_2$-Tl_2SnSe_3-TlSe-Se*. Journal of the Less-Common Metals, *81*, (1981) 181–197. 22

[Howarth53] D. J. Howarth and E. H. Sondheimer. In *Proceedings of the Royal Society of London*, volume A219. 1953. 12

[Ioffe57] A. F. Ioffe, L. S. Stil'bans, E. K. Iordanishvili and T. S. Stavitskaya. *Thermoelectric Cooling*. In *Semiconductor Thermoelectric Devices and Materials*. Infosearch, London, 1957. 6

[Jones98] C. D. W. Jones, K. A. Reagan and F. J. DiSalvo. *Thermoelectric Properties of the Doped Kondo Insulator: $Nd_xCe_{3-x}Pt_3Sb_4$*. Physical Review B, *58*, (1998) 16057–16063. 61

[Jones99] C. D. W. Jones, K. A. Reagan and F. J. DiSalvo. *$Ce_3Cu_xPt_{3-x}Sb_4$: Modifying the Properties of a Kondo Insulator by Substitutional Doping*. Physical Review B, *60*, (1999) 5282–5286. 61

[Keyes59] R. W. Keyes. *High-Temperature Thermal Conductivity of Insulating Crystals: Relationship to the Melting Point*. Physical Review, *115*, (1959) 564–567. 14

[Larson99] P. Larson, S. D. Mahanti, S. Sportouch and M. G. Kanatzidis. *Electronic Structure of Rare-Earth Nickel Pnictides: Narrow-Gap Thermoelectric Materials*. Physical Review B, *59*, (1999) 15660–15668. 51, 52, 54, 56

[Latypov88] Z. M. Latypov, N. R. Faizullina, R. N. Sagitov and V. P. Savel'ev. *The Tl_4PbSe_3–Tl_4PbTe_3 System*. Izvestiya Akademii Nauk SSSR, Neorganicheskie Materialy, *24*, (1988) 1920–1921. 23

[Mahan97] G. D. Mahan. *Good Thermoelectrics*. In *Solid State Physics — Advances in Research and Applications* (edited by H. Ehrenreich and F. Spaepen), volume 51, pages 81–157. Academic Press, 1997. 15, 41

[Nordell96] K. J. Nordell and G. J. Miller. *Electronic Structure, Superconductivity and Substitution Patterns in Tl_5Te_3*. Journal of Alloys and Compounds, *241*, (1996) 51–62. 21, 22

[Peltier34] J. C. Peltier. *Nouvelles experiences sur la caloricite des courans electrique*. Annales de chimie, *LVI*. 5

[Pradel82] A. Pradel, J.-C. Tedenac, D. Coquillat and G. Brun. *Propriétés Thermoélectriques de Tl_9BiTe_6*. Revue de Chimie Minerale, *19*, (1982) 43–48. 23

[Schewe89] I. Schewe, P. Böttcher and H. von Schnering. *The Crystal Structure of Tl_5Te_3 and its Relationship to the Cr_5B_3 Type*. Zeitschrift für Kristallographie, *188*, (1989) 287–298. 21

[Seebeck22] T. J. Seebeck. *Magnetische Polarisation der Metalle und Erze durch Temperatur-Differenz*. Abhandlungen der Deutschen Akademie der Wissenschaften zu Berlin, page 265. 5

[Seeger99] K. Seeger. *Semiconductor Physics: An Introduction*. Springer Verlag, Berlin, 1999, 7th edition. 26, 44

[Shockley50] W. Shockley. *Electrons and Holes in Semiconductors*. Bell Laboratories Series. Van Nostrand, New York, 1950. With Applications to Transistor Electronics. 12

[Slack79] G. A. Slack. *The Thermal Conductivity of Nonmetallic Crystals*. In *Solid State Physics — Advances in Research and Applications* (edited by H. Ehrenreich, F. Seitz and D. Turnbull), volume 34, pages 1–71. Academic Press, 1979. 15

[Spears01] B. Spears. *Britney's Guide to Semiconductor Physics* (2001). `http://britneyspears.ac/lasers.htm`. 8

[Sportouch99] S. Sportouch, P. Larson, M. Bastea, P. Brazis, J. Ireland, C. R. Kannewurf, S. D. Mahanti, C. Uher and M. G. Kanatzidis. *Observed Properties and Electronic Structure of RNiSb Compounds (R = Ho, Er, Tm, Yb and Y). Potential Thermoelectric Materials*. In *Thermoelectric Materials 1998 — The Next Generation Materials for Small-Scale Refrigeration and Power Generation Applications* (edited by T. M. Tritt, M. G.

Kanatzidis, G. D. Mahan and J. Hylan B. Lyon), Symposium Proceedings, pages 421–433. Materials Research Society, 1999. 51, 54, 55, 59, 71

[Thomson51] W. Thomson. *On a Mechanical Theory of Thermoelectric Currents*. Proceedings of the Royal Society of Edinburgh, page 91. 5

[Vegard21] L. Vegard. *Die Konstitution der Mischkristalle und die Raumfüllung der Atome*. Zeitschrift für Physik, *5*, (1921) 17–26. 32

[Villars91] P. Villars and L. D. Calvert (editors). *Pearson's Handbook of Crystallographic Data for Intermetallic Phases*. ASM International, 1991. 21

[Wang99] M. Wang, R. McDonald and A. Mar. *$M_3Ni_3Sb_4$ ($M = Zr$, Hf) and $Zr_3Pt_3Sb_4$. Ternary Antimonides with the $Y_3Au_3Sb_4$ Structure*. Inorganic Chemistry, *38*, (1999) 3435–3438. 61

[Weast84] R. C. Weast, M. J. Astle and W. H. Beyer (editors). *CRC Handbook of Chemistry and Physics*. CRC Press, Boca Raton, FL, 1984, 65th edition. 42, 58

[Wolfing00] B. Wölfing. *Tl_9BiTe_6: A New Thermoelectric Material with Record Efficiencies*. Ph.D. thesis, Universität Konstanz (2000). i, iii, 2, 21, 22, 23, 25, 26, 29, 30, 31, 33, 41, 42

[Wood88] C. Wood. *Materials for Thermoelectric Energy Conversion*. Reports on Progress in Physics, *51*, (1988) 459–539. 13

[Ziman60] J. Ziman. *Electrons and Phonons: The Theory of Transport Phenomena in Solids*. Clarendon, 1960. 30

Acknowledgements

This work was only possible with the help of many people, who supported me in several different ways. In particular, I want to thank

- Prof. Dr. Ernst Bucher for the opportunity to do most of my work in his laboratory at Bell Labs. In many insightful discussions I learned a lot from him about solid-state physics and science in general.
- Prof. Dr. Peter Wyder for being the co-advisor of this work.
- Bernd Wölfing for mentoring me during my work here. He did not only teach me everything about thermoelectricity and about the work in the lab, he also helped me with so many private things and was a real friend.
- Christian Kloc for an uncountable number of discussions, not only about physics, but also about work, people and living in the US. He was the one who always found an easy solution when I was stuck with an experimental problem.
- Hendrik Schön and Ralph Spolenak for having a lot of fun in the US. With both of them I had many interesting discussions, as they seem to know everything about physics.
- Many friends and colleagues here in America for a great time not only in the Murray Hill office, but also in the "Office" in Summit and in many other places in New Jersey and in New York City.
- All my friends back in Germany who accompanied me during my studies in Konstanz. I had a great time there and learned a lot with and from them.
- Very special thanks to my parents. Even after the motorcycle accident of my father, and after I left them alone to go to America, they greatly supported me and never let me feel alone.

Index